SLAC-360
UC-414
(E)

PROPERTIES OF HADRONIC DECAYS OF THE Z BOSON*

Kathryn F. O'Shaughnessy

Stanford Linear Accelerator Center
Stanford University
Stanford, California 94309

June 1990

Prepared for the Department of Energy
under contract number DE-AC03-76SF00515

Printed in the United States of America. Available from the National Technical Information Service, U.S. Department of Commerce, 5285 Port Royal Road, Springfield, Virginia 22161. Price: Printed Copy A07, Microfiche A01.

* Ph.D. thesis

Abstract

The decays of the Z^0 boson to quarks and subsequently to hadrons were first directly observed in 1989 with the Mark II detector. This report studies the general properties of the hadronic events in the initial data sample recorded at center-of-mass energies near the Z^0 resonance (91.2 GeV).

The preliminary chapters introduce the theoretical framework and the apparatus. A brief review is given of some features of Quantum Chromodynamics (QCD) that are relevant to the study. Two QCD–based models that are used to help correct the data distributions for detector effects and also for comparisons with the corrected distributions are described. For each of the detector systems used in the analysis, the design, operation and performance is discussed.

The next chapter describes the event selection which is designed to provide a sample of well-measured hadronic events. The following three chapters contain the measured data distributions. The QCD–based models with parameters tuned at E_{cm}= 29 GeV describe the 91 GeV data distributions well. Each of these chapters also shows the variation of the observables as the center-of-mass energy changes.

The event shape variables chosen for study are sphericity, aplanarity, thrust, and the hemisphere invariant masses. The distributions at 91 GeV show that the majority of the events are 2–jet-like, with most of the energy confined to two narrow cones

around an axis. However, there is a significant number of events with considerable momentum away from this axis; those topologies are attributed to events with gluon radiation from the primary quarks.

The jet analysis begins with a description and comparison of two widely used jet cluster algorithms. One of them is chosen to apply to the data, and the number of jets as a function of the jet resolution parameter is measured.

The last topic consists of a study of the individual charged-particle track momenta. The corrected charged multiplicity is derived and then compared with lower energy values. The charged-particle inclusive distributions shown are those of the scaled momentum, the transverse momenta to the sphericity axis in and out of the event plane, and the rapidity.

Acknowledgements

My time at Stanford has been a true learning experience. I would like to thank the Natural Sciences and Engineering Research Council of Canada and the US Department of Energy for providing the financial support for my work here. In addition, many people contributed to the experience both academically and socially; I would like to acknowledge their support.

Firstly, I would like to thank the Mark II collaboration for providing a wonderful environment to learn about particle physics. I would like particularly like to thank the technical staff at SLAC who have patiently and good-naturedly taught me much about the hardware aspects of a detector. I would like to list all of the physicists who have shared their ideas and listened to mine but our author lists are long enough. However, some people deserve special mention. I would like to thank Gary Feldman, my advisor; John Bartelt, my office-mate, for answering innumerable questions; Dave Coupal, Jordan Nash, Tricia Rankin and Rick Van Kooten for making work on the FADC system so enjoyable; and Walt Innes and Tom Glanzman for passing on their knowledge about the detector so cheerfully.

For encouraging me to join activities away from SLAC, I would like to acknowledge my friends and fellow grad students in the Physics and Applied Physics Departments over the years. Also the students and staff at the International Center and the

members of the Dunai folk dance ensemble who helped me realize that there was more to being here than academics.

Finally, I would like to thank my family for their continued support and encouragement of my seemingly endless academic career. Especially my husband and "coach", Jerry, whose love and companionship has made these last few years much richer.

Contents

List of Tables

List of Figures

Chapter 1

Introduction

The Z^0 boson is a recent addition to the list of observed elementary particles. A mediator of the weak force, it was postulated in 1967 [1] and the first experimental evidence for it was seen in proton–anti-proton collisions at the CERN laboratory near Geneva, Switzerland, in 1983. The UA1 [2] and UA2 [3] experiments recorded events where the reactions $Z^0 \rightarrow e^+e^-$, $\mu^+\mu^-$ took place.

However, the more copious decays of the Z^0, namely to quarks, are too difficult to extract from other processes happening at proton accelerators. Therefore two laboratories, SLAC at Stanford, CA and CERN, undertook to build machines that would produce Z^0 particles through e^+e^- annihilation. The SLAC Linear Collider (SLC) was a prototype of a new type of accelerator; the CERN facility (LEP) was a conventional storage ring accelerator at a large scale. Both machines started collecting data in 1989. The first SLC events were recorded by the Mark II detector in April [4] and the four detectors at LEP (ALEPH, DELPHI, L3 and OPAL) [5] all recorded events during a short run in August and September.

Between the time that the Z^0 was first discovered and the first Z^0 events were

produced at SLC and LEP, a tremendous number of studies had been made by both theorists and experimentalists. The interactions of the Z^0 with other particles were predicted and the information that could be inferred about the basic theories of matter from Z^0 measurements was studied [6]. It was found that Z^0 decays are a rich place to look for new particles, to make precision tests of predictions of the theories, and to learn more about areas where the theories cannot yet make predictions.

This report examines a narrow part of the second two categories. The data sample was collected by the Mark II detector at the SLC. The general properties of the decays of the Z^0 boson to quarks have been studied, concentrating on the effects of the strong interaction which is one of the three forces that are combined in what is called the Standard Model. The rest of this chapter explains the Standard Model and what might be learned about the strong interaction by studying hadronic decays of the Z^0.

Chapter 2 describes the physics models that are used to simulate hadronic decays and Chapter 3 discusses the general features of the Mark II detector. The method that is used to select hadronic events based on detector measurements is described in Chapter 4. Chapters 5–7 contain the results of the analysis, loosely divided into the topics of event shapes, jet studies, and charged-particle inclusive studies. Chapter 8 summarizes the findings of the analysis.

1.1 Theory

It is well beyond the scope of this report to detail the complete theoretical framework which supports the current beliefs of particle physics. In fact, only a brief summation is offered of the concepts that affect the analysis. For more comprehensive reviews, see [7].

Table 1: Matter-building particles in the Standard Model.

Quarks [Masses (GeV)]			Charge (e)
up (u)	charm (c)	top (t)	$+2/3$
[0.005]	[1.4]	[> 72]	
down (d)	strange(s)	bottom (b)	$-1/3$
[0.007]	[0.150]	[4.8]	
Leptons [Masses (GeV)]			
electron (e^-)	muon (μ^-)	tau(τ^-)	-1
[0.00051]	[0.1056]	[1.784]	
e^- neutrino (ν_e)	μ^- neutrino (ν_μ)	τ^- neutrino (ν_τ)	0
[$< 0.46 \times 10^{-7}$]	[$< 0.50 \times 10^{-3}$]	[< 0.164]	

1.1.1 Standard Model

The successful theory that integrates the electromagnetic force, the weak nuclear force and the strong nuclear force is called the Standard Model. The first step in building the model was the unification of the first two forces into the electro-weak theory. This was accomplished by Glashow [8], Weinberg [1], and Salam [9] by combining the gauge symmetry of the weak interaction, denoted SU(2) (special unitary group with 2 dimensions) with U(1) (unitary group with dimension 1) which described electromagnetic interactions. Adding the similar gauge group description of the strong interaction, SU(3), then provides a mathematical formulation of the three forces.

In the model there are two types of matter-building particles, quarks and leptons, as well as force-mediating particles. The quarks and leptons are postulated to be grouped into "generations" as shown in Table 1[1]; the different types of quarks are said to be different "flavors". Also shown in the table are the electric charge of each

[1]The Standard Model sets the number of generations to 3, but many wondered if there were more generations at heavier masses. One of the analyses of the Z^0 data has shown that the number of generations with light neutrinos is less than 3.9 at a 95% confidence level [10], excluding a 4^{th} similar generation.

particle and the masses (or, if not known, mass limits). Of the particles listed, the top quark has not been experimentally verified [11]. Each particle in the table has a corresponding anti-particle partner that is not shown. The quantum numbers (*e.g.* charge) are the opposite in sign for the anti-particle. The spin quantum numbers of the quarks and leptons are half-integers, therefore they obey Fermi-Dirac statistics and are called fermions.

The particles that mediate the forces are shown in Table 2. They have integral spins and so are members of the class called bosons (they obey Bose-Einstein statistics). Another boson that is part of the Standard Model is called the Higgs boson. Its presence is a result of the mechanism to generate masses for the particles.

1.1.2 The Z^0 Boson

The Z^0 boson, a mediator of the weak force, is the heaviest of the mediating particles in the Standard Model. Its mass has been determined to be 91.14± 0.14 GeV [10]. It is neutral and can decay into any fermion–anti-fermion pair with a combined mass less than its mass (therefore all particles in Table 1 except the top quark). Table 3 shows the relative decay fractions of the Z^0 to the various quarks and leptons. The ability to observe the decay of the Z^0 into quarks substantially increases the possibilities for studying the properties of the Z^0.

Table 2: The three forces described by the Standard Model and the gauge bosons that mediate them.

Force	Mediating particle
Electromagnetic	photon (γ)
Weak	intermediate vector bosons ($W^{\pm}, Z^0$)
Strong	gluon (g)

Table 3: Relative decay fractions of the Z^0 to the fermions.

Decay Mode	Percent of Decays
$\nu_e\bar{\nu}_e, \nu_\mu\bar{\nu}_\mu, \nu_\tau\bar{\nu}_\tau$	6.1%
$e^+e^-, \mu^+\mu^-, \tau^+\tau^-$	3.1%
$u\bar{u}, c\bar{c}, t\bar{t}$	10.6%
$d\bar{d}, s\bar{s}, b\bar{b}$	13.6%

The Z^0 is produced by the annihiliation of an electron (e^-) and its anti-particle, the positron (e^+). The cross section for producing the Z^0 peaks at center-of-mass energies near the Z^0 mass; at lower energies, e^+e^- annihilation results in the production of an intermediary photon. As both the Z^0 and photon are neutral mediators of the electroweak force, they both decay to fermion–anti-fermion pairs (although with different couplings). Thus we can compare the general hadronic properties of the Z^0 decays directly with those from e^+e^- annihilation experiments. An advantage to studying Z^0 decays is that the produced particles have higher energies.

A physics process which affects e^+e^- annihilation is the radiation of a photon by the initial e^- or e^+; the process is called initial state radiation. The result is a lowering of the energy available to produce the intermediate state. In the case of e^+e^- annihilation at E_{cm}= 29 GeV, the radiated photons could have energies of several GeV. Monte Carlo (MC) programs were developed so that the energy loss could be predicted. The presence of the Z^0 boson resonance makes the effect less important. If beam energies are set to run near the peak of the resonance and either of the initial particles emits an energetic photon, the center-of-mass energy drops below the Z^0 mass where the interaction cross section is small. So these events are rare. In any case, the process is included in the MC simulations and a correction is made.

1.1.3 Quantum Chromodynamics

This report will be investigating particles interacting via the strong nuclear force. The theory that describes the interaction is called Quantum Chromodynamics (QCD). The charge carried by the particles is known as color, of which there are 3 (typically labelled red, yellow and blue). The non-abelian nature of the theory means that the force carriers, the gluons, also carry color and can self-interact; this has interesting consequences.

One of the consequences is quark confinement. The gluon self-interaction causes the force between quarks to be very strong and to rise linearly with distance. As a quark is pulled away from other quarks (or any strongly interacting particles) a large amount of energy is contained in the field between them and new quarks are produced from that energy. Thus we observe combinations of quarks, not single ones. These combinations are called hadrons and are divided into mesons (a quark and an anti-quark) and baryons (three quarks together). An important part of QCD analyses is estimating the effects of only observing hadrons, not the quarks and gluons.

Another consequence is seen when the coupling constant, α_s, is examined. The bare coupling constant, α_{so}, is defined at the vertex shown in Figure 1a. Higher order corrections to the vertex, such as the type shown in Figure 1b, cause the value of α_{so} to change, so a value different from the bare coupling constant is measured by experiments. To avoid infinities in the calculation and to determine the relationship between α_{s0} and α_s, we perform a renormalization procedure and specify an energy Λ which is a reference point. A result is that the value of α_s depends on the energy at which it is being measured. To second order, the coupling constant is calculated as:

$$\alpha_s(q^2) = \frac{12\pi}{b_0 \ln(q^2/\Lambda^2) + b_1/b_0 \ln(\ln(q^2/\Lambda^2))},$$

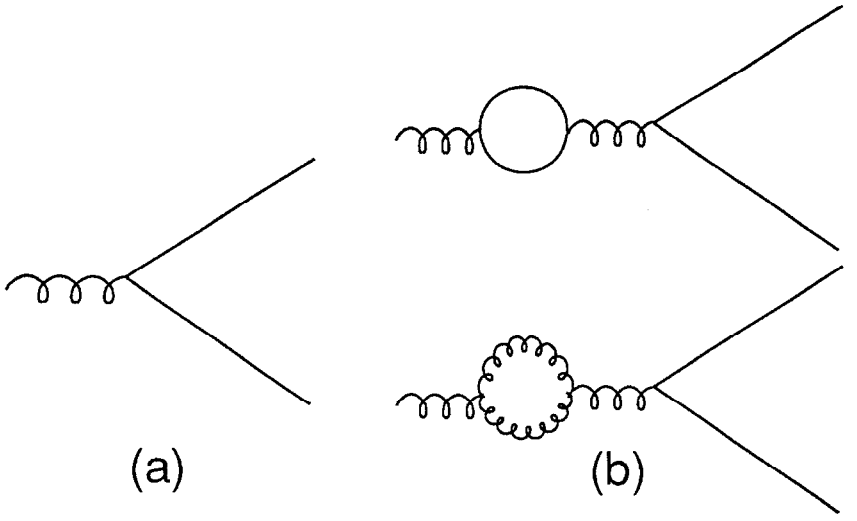

Figure 1: Diagrams involved in the definition of α_s: a) the simple vertex b) some higher order corrections to the vertex.

where

$$b_0 = (33 - 2n_f)$$

$$b_1 = (918 - 114n_f)$$

and n_f is the number of flavors produced at the q^2 being studied. The parameter Λ represents the renormalization point (the energy at which α_s becomes infinite) and its value depends on the renormalization scheme. A widely used scheme is the modified Mimimal Subtraction scheme ($\overline{MS}$) and the corresponding parameter is usually labelled $\Lambda_{\overline{MS}}$. The value of $\Lambda_{\overline{MS}}$ must be determined from experiment.

If n_f is less than 16 (which is very likely) then b_0 is positive and as q^2 increases, α_s decreases. This trend is termed the "running" of α_s and is much more visible here than in the corresponding description of the electromagnetic force. The difference comes from the gluon self-interaction contributions to the diagrams. At very high energies ($q^2 \to \infty$), $\alpha_s(q^2) \to 0$ and the strong interaction between quarks and gluons

is negligible. This effect has been termed "asymptotic freedom" [12] and implies that perturbation theory can be used at high energies. The energy scale for the division between the perturbative region and the non-perturbative region is set by Λ; an experimental value was measured by Mark II was $\Lambda_{\overline{MS}} = 0.29^{+0.17+0.11}_{-0.12-0.06}$ GeV using SLC data and $\Lambda_{\overline{MS}} = 0.28^{+0.02+0.08}_{-0.02-0.07}$ GeV using PEP data [13].

Chapter 2

QCD Models

The models described in this chapter simulate the general characteristics of hadronic events. For a given set of parameters, each model will provide a set of events listing particles and their momenta and energies. Choices about the content of individual events are made probabilistically. Some of the parameters are determined by the experimental situation or are known numbers (*e.g.* beam energy and particle masses) and others are inherent to the particular model.

This chapter outlines the general features of models and then discusses the two models used later in more detail.

2.1 Purpose of the Models

QCD models play an important part in experimental high energy physics. In most currently running experiments, quark interactions are a large part of the physical processes that are occurring. Being able to simulate these interactions and the resulting particles have the following uses.

As discussed in the next section, the simulation of hadronic events is usually

divided into two energy regions. In the first region, at high energies, calculations of probabilities of momentum configurations have been made. The results of those calculations are implemented in the models using Monte Carlo techniques, and predict the behavior of the quarks and gluons. These predictions should be measured to test the theory of QCD.

The second energy region describes the transformation of quarks and gluons (partons) to the measured hadrons. The process is not calculable using available techniques, so the production of hadrons (known as "fragmentation") must be modelled. For analyses which are trying to probe the behavior of partons, it is necessary to investigate the effects of the fragmentation. In some cases, the parton information is masked by the hadrons (*e.g.* trying to determine the direction of a quark from the resulting hadrons (see section 6.1.2)). Many analyses turn to the models to estimate the fragmentation effects. In addition, if the fragmentation models are based on physics principles, the comparison of data and the models may lead to a greater understanding of hadron production.

As well as the possibility of the models providing deeper insight to QCD and testing its predictions, the models are also a useful tool for experimenters. Each quantity that is measured is affected by the detector measuring it. To correct for this, Monte Carlo simulations of the detector are written which use the particles generated by the QCD-based models as the starting point. The detector simulation in some ways can be thought of as a third stage of the model.

Although QCD does not often give predictions of the values of observables, it can in some cases predict the energy evolution. When implemented in the models, this allows the prediction of the data environment, which can have implications for detector design. For example, at the SLC the predictions of particle multiplicities

and separations helped establish criteria for track separation in the tracking devices designed.

2.2 Two Energy Regions

The large size of the coupling constant α_s at low energies means that the event simulation must be divided into two regions. The division occurs because of the calculational tools available (or lacking) to make predictions from QCD.

2.2.1 Perturbative

In the first region, the perturbative region, the quarks have such large energies that the coupling constant is relatively small ($\approx O(0.10)$) and so quark production can be calculated using a perturbative series with the nth term preceeded by a coefficient of α_s^n. Thus each successive term becomes smaller and so terminating the series or making approximations is possible.

There are two methods which are currently used to produce the partons. The first method, the matrix element method, uses calculations of the coefficients of the perturbative expansion to estimate the number and 4-momenta of the produced partons. At this point, only terms up to $O(\alpha_s^2)$ have been calculated and confirmed and so at most 4 partons can be produced (see Figure 2). The calculations usually make varying assumptions (such as the procedure to recombine soft gluons) and hence some uncertainty is introduced at this level.

The other method is to keep the leading log terms to all orders and so it is called the leading log approximation (LLA). In the models, it can be implemented as a showering or cascading mechanism (see Figure 3), where at each branching a

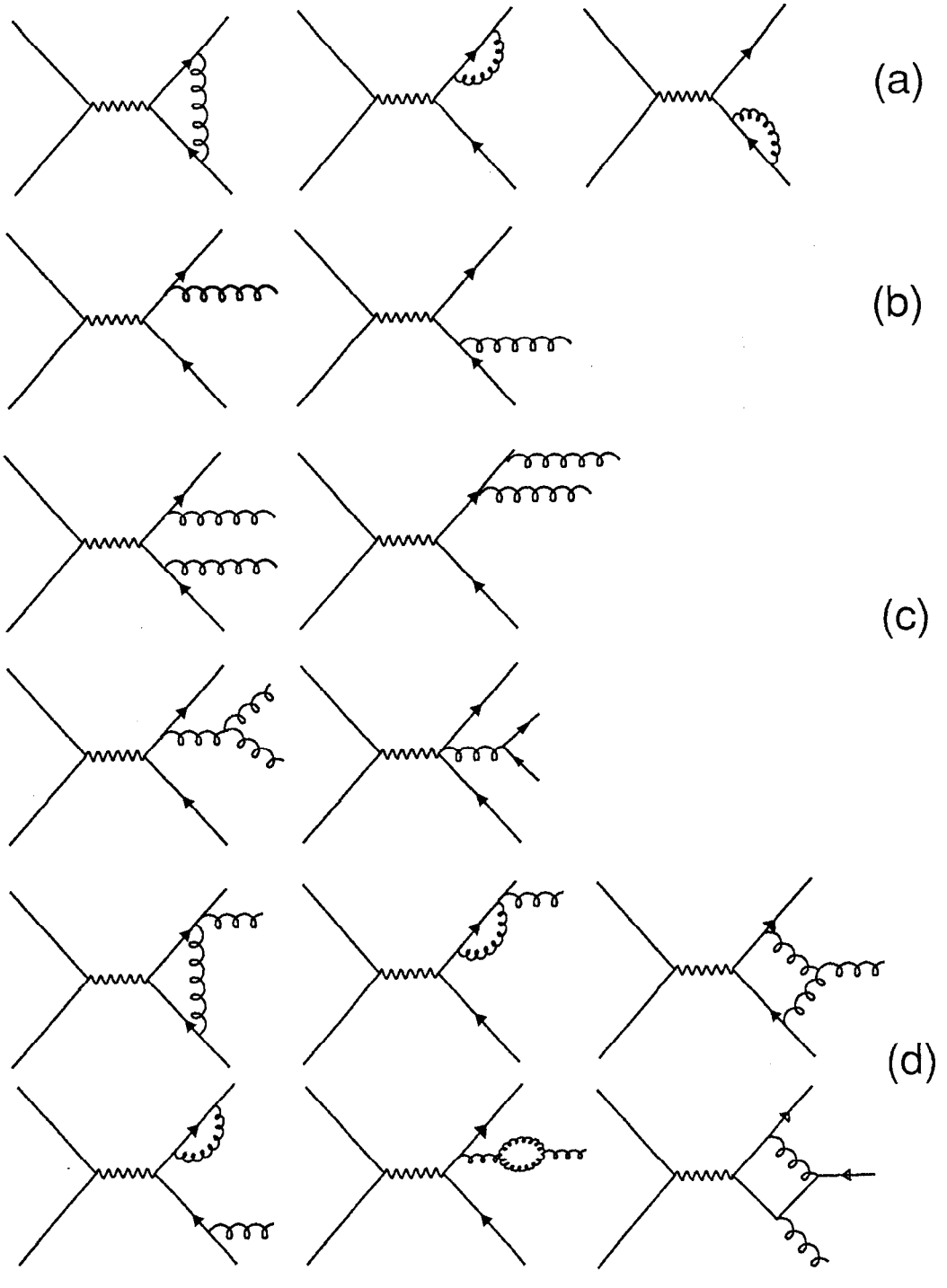

Figure 2: Feynman diagrams for parton generation: (a) first order corrections to $q\bar{q}$ (b) first order $q\bar{q}g$ production (c) second order $q\bar{q}q'\bar{q}'$ or $q\bar{q}gg$ production and (d) some diagrams contributing to second order corrections to $q\bar{q}g$.

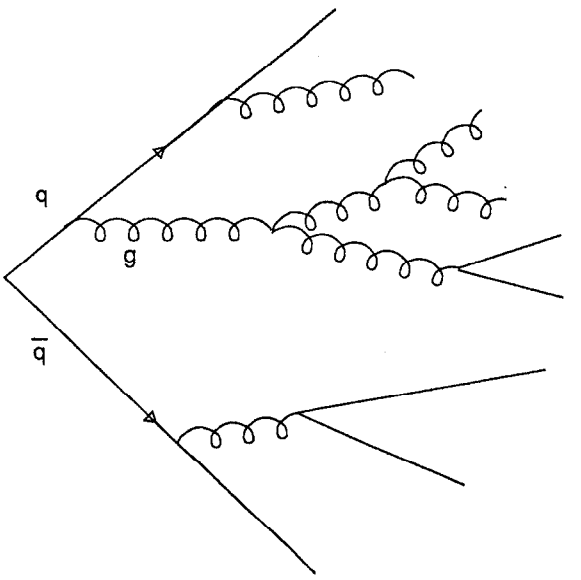

Figure 3: Conceptual view of a parton shower.

statistical determination of the amount of momentum carried by the products is used. This calculation is a good approximation in the case where the available energy is quickly decreasing at each branching point.

2.2.2 Fragmentation

The second region of the simulation is at a low enough energy that the quarks undergo "hadronization" or "fragmentation", that is, the confinement property causes other quarks to be produced and hadrons to form. These hadrons are given some of the characteristics and properties of the parent parton. Because the coupling constant is so large at these energies, none of the calculational tools above can be used and so models must be employed. The initial particles are a set of generated partons with known 4-momenta. The models then use ideas based on physics principles, but not necessarily calculations, to produce the primary hadrons.

The first models used what is now called independent jet fragmentation to form hadrons [14]. As a quark moves out from the production point, $q\bar{q}$ pairs are produced with some fraction of the original quark's momentum. One of these quarks will pair with the original quark and the other will continue on. This process continues iteratively until the remaining quark has very little energy. The product quarks are treated the same as the first quark, with no influence from previous branchings in the chain or from other quarks (hence the description independent). Several experimental measurements suggest that this assumption is not valid [15] and therefore independent jet fragmentation is regarded as less accurate than some of the later models[1]. It will not be discussed further in this report.

The available information about the forces between quarks suggests that the confining part of the strong force, F_s, is governed by a term

$$F_s \propto k\, r$$

where r is the distance between the quarks and k is a constant. This is the same relationship for the force due to a string, and a model was derived [17] where the quarks are pictured as endpoints of a string. As the quarks move apart, the string has more energy and eventually will "break", creating two more quarks as endpoints. This process continues until there is too little energy in the string to create more quarks. The string then decays to hadrons. This method is known as string fragmentation, or Lund fragmentation (from the group at Lund University that developed it).

The cluster fragmentation method takes the result of the perturbative parton generation and forms colorless clusters of quarks. The clusters then decay according to phase space. In later versions of the models heavy clusters decay using a string

[1] A recent paper [16] claims than an adjustment of the treatment of soft particles can reproduce the data, and that the independent fragmentation model is a viable model.

mechanism to smaller clusters before undergoing the usual cluster decay.

2.3 Specific Models and their Implementation

The previous section briefly outlined the general concepts of the models. This section describes the implementation of two of the more widely used QCD models. By necessity the discussion will be brief; these models have become very complex programs. References [18] contain excellent reviews and comparisons of the programs.

2.3.1 BIGWIG 4.1

This model is based on ideas by Webber and Marchesini [19] and uses a parton shower generation (the leading log approximation) and cluster fragmentation. It was the first widely used model to use showering to generate partons.

The initial quark flavor is chosen based on the probability of coupling to the Z^0. The kinematic variables used in the showering require the choice of a reference frame and the BIGWIG authors have chosen a frame where the initial two partons have an opening angle of 90°. Version 4.1 also uses $O(\alpha_s)$ calculations to weight the momenta of this first splitting. It was found that this technique compensated for a tendency of the shower parton generation to underestimate hard gluon radiation. The momenta for the subsequent branchings of these partons (emitting gluons or the gluons branching to $q\bar{q}$ pairs or to two gluons) are governed by the Altarelli-Parisi equations [20]. The strength of the coupling constant α_s at each branching depends on the parameter Λ as shown in Chapter 1. The evaluation of Λ depends on the calculational scheme used, in this case the leading log approximation, so we label the model parameter Λ_{LLA}. Coherence between gluons is included by a requirement

that each succeeding opening angle be smaller than the previous one. The branching process continues until the partons have energy below some cutoff parameter Q_0 (all the partons are considered massless at this point).

The cluster fragmentation is then implemented. Remaining gluons are forced to break into $q\bar{q}$ pairs, and all of the quarks and anti-quarks are paired together to form colorless clusters. An improvement over earlier versions is that if the cluster is heavier than M_c, then the cluster fragments using a string-like mechanism before the regular cluster decay is used. Within a cluster, a new flavor q' is chosen, and the resulting two hadrons from the cluster will be $q\bar{q}'$ and $\bar{q}q'$. The choice of isospin and angular momentum for the hadron (*e.g.* whether a $u\bar{u}$ combination will be a π^0 or a ρ^0) is weighted by the number of possibilities. These hadrons then decay according to their known decay properties. Energy and momentum conservation are forced at the end of the generation by working backwards along the chain.

The mechanism described above only allows the creation of mesons ($q\bar{q}'$ pairs), whereas we know baryons (groups of three quarks or anti-quarks) are also produced in e^+e^- annihilation. The BIGWIG model forms baryons in two ways. The first is to allow gluons to branch to diquark–anti-diquark pairs during the shower. The second is to allow the flavor q' chosen during the cluster decay to be a diquark. With these mechanisms, the BIGWIG model has been able to describe the observed baryon production in the data [21].

2.3.2 JETSET 6.3

The JETSET model [22], often called the Lund model because it features the string fragmentation developed there, has two different options for parton generation. The default is to use $O(\alpha_s^2)$ matrix element calculations of the type described above.

For the implementation used at Mark II, the calculations by Gutbrod, Kramer, and Schierholz (GKS) [23] are used to predict the number and momenta of the partons. Again a parameter Λ is needed to define α_s; in this case it is denoted $\Lambda_{\overline{MS}}$. In addition, for the calculations to remain finite when soft gluons are emitted, a parton pair resolution parameter y_{min} is used. This parameter dictates the minimum scaled invariant mass between two partons; $y_{min} = m^2_{min}/s$, where $s = {E_{cm}}^2$. The advantage of using the matrix elements to predict parton production is that they are calculated using well-established methods and are reliable as long as the coefficients of the higher order corrections are small. However, they can at most give 4 partons and there are indications that this is not adequate to describe the data at 91 GeV [21].

The version of JETSET 6.3 that uses parton shower generation has become one of the more successful models for describing recent e^+e^- data [21,24]. The showering mechanism for version 6.3 is slightly different in detail from BIGWIG 4.1; the amount of momentum the daughter particles receive at the branching is defined differently. Also, JETSET considers the masses of the partons at each step whereas BIGWIG calculates the masses of the partons after the cascade has finished. These differences lie more in the implementation details rather than the fundamental idea of the shower picture. The parameters Λ_{LLA} and Q_0 serve the same functions as the equivalents in the BIGWIG model.

The fragmentation parameters for the string fragmentation have the same definition but will have different values for the two parton generation schemes since the parton configuration going into the hadronization stage is different. The fragmentation function, which governs the momentum sharing of the two quarks at a break in the string, is given by

$$f(z) = \frac{1}{z}(1-z)^a exp(\frac{-bm_T^2}{z}).$$

The quark direction is used in the definition of $z = E + p_{\|}$, $m_T = \sqrt{p_T^2 + m^2}$ is the transverse mass of the hadron and a, b are the parameters to be determined by fits to the data. The transverse momenta of the hadrons is given by a Gaussian function with width σ.

2.4 Parameters

The parameters of the models are in some cases well fixed by the experimental situation (*e.g.* beam energy) and in other cases must be determined from the data. Although the choice of values for the parameters seems to have a large range, it is usually possible to tune them by choosing a judicious set of data distributions that are sensitive to changes. This procedure was performed by Mark II [24] and TASSO [25], among other experiments, using data collected at 29 GeV and 35 GeV, respectively. The distributions used were the same types as those studied in this analysis, therefore it is known that they are well matched by the models at lower energies. In Table 4 are shown the values obtained in the two studies for the two models. For this report, the Mark II parameters tuned at 29 GeV are used for model comparisons. If the energy variations are built into the models properly, they should be able to predict the distributions at 91 GeV with no changes.

The difficulty with this philosophy is that a parameter for the JETSET matrix element model cannot be sensibly used at 91 GeV. The parameter in question is the minimum invariant mass, y_{min}, which has a tuned value of 0.015. Physically the parameter is describing the point at which we cannot resolve a soft gluon from another parton. Practically, it is a cutoff to avoid singularities in the calculation. It defines an absolute energy scale for the invariant mass of the partons. The remaining energy

Table 4: Parameters for the QCD Monte Carlo models used.

Parameter	Mark II value	TASSO value
JETSET 6.3 $O(\alpha_s^2)$		
$\Lambda_{\overline{MS}}$ QCD scale	0.5	0.62
y_{min} cutoff for combining partons	0.015	0.02
A frag function	0.9	0.58
B frag function	0.7	0.41
σ_q for $p_\perp$	0.265	0.40
JETSET 6.3 shower		
Λ_{LLA} QCD scale	0.4	0.26
Q_0 cutoff for parton evolution	1.0	1.0
A frag function	0.45	0.18
B frag function	0.9	0.34
σ_q for $p_\perp$	0.23	0.39
BIGWIG 4.1		
Λ_{LLA} QCD scale	0.75	0.25
Q_0 cutoff for parton evolution	0.75	0.61
M_c for cluster cutoff	3.0	2.3

is handled by the fragmentation process and the parameters a and b. Therefore as E_{cm} changes, m_{min} should be kept fixed in order to use the same values for a and b. The corresponding value of y_{min} at 91 GeV is 0.0015, at which point the calculations give an unphysical negative number of 2–jet events. So the parameters tuned at 29 GeV cannot be used to generate events at 91 GeV. With the data sample presently available, it is not possible to retune the parameters to the data; therefore this version of the model cannot be used for comparison with the Z^0 hadronic data.

Chapter 3

Apparatus

The Mark II detector was upgraded in preparation for its role as the first detector to take data at the SLAC Linear Collider (SLC) [26]. The SLC provides colliding electron and positron beams at a center-of-mass energy of roughly 91 GeV. It is the first prototype of the linear collider type of accelerator. Typical running luminosities during the data-taking for the analysis of this report were on the order of 10^{28} $cm^{-2}s^{-1}$. The SLC has only one collision point which the Mark II detector has occupied since 1986.

A schematic view of the detector can be seen in Figure 4. Emerging from the interaction point (IP), a particle emitted perpendicular to the beam would traverse the beampipe, the central drift chamber, a time-of-flight counter, the coil of the solenoid magnet, the liquid argon calorimeter and finally the muon detection system. At low angles, coverage is provided by the endcap calorimeter and the small-angle monitor. The following sections describe the components used for the analysis. In several cases, the performance of the components as measured at PEP is quoted; the data sample at SLC energies is not large enough to provide a statistically meaningful

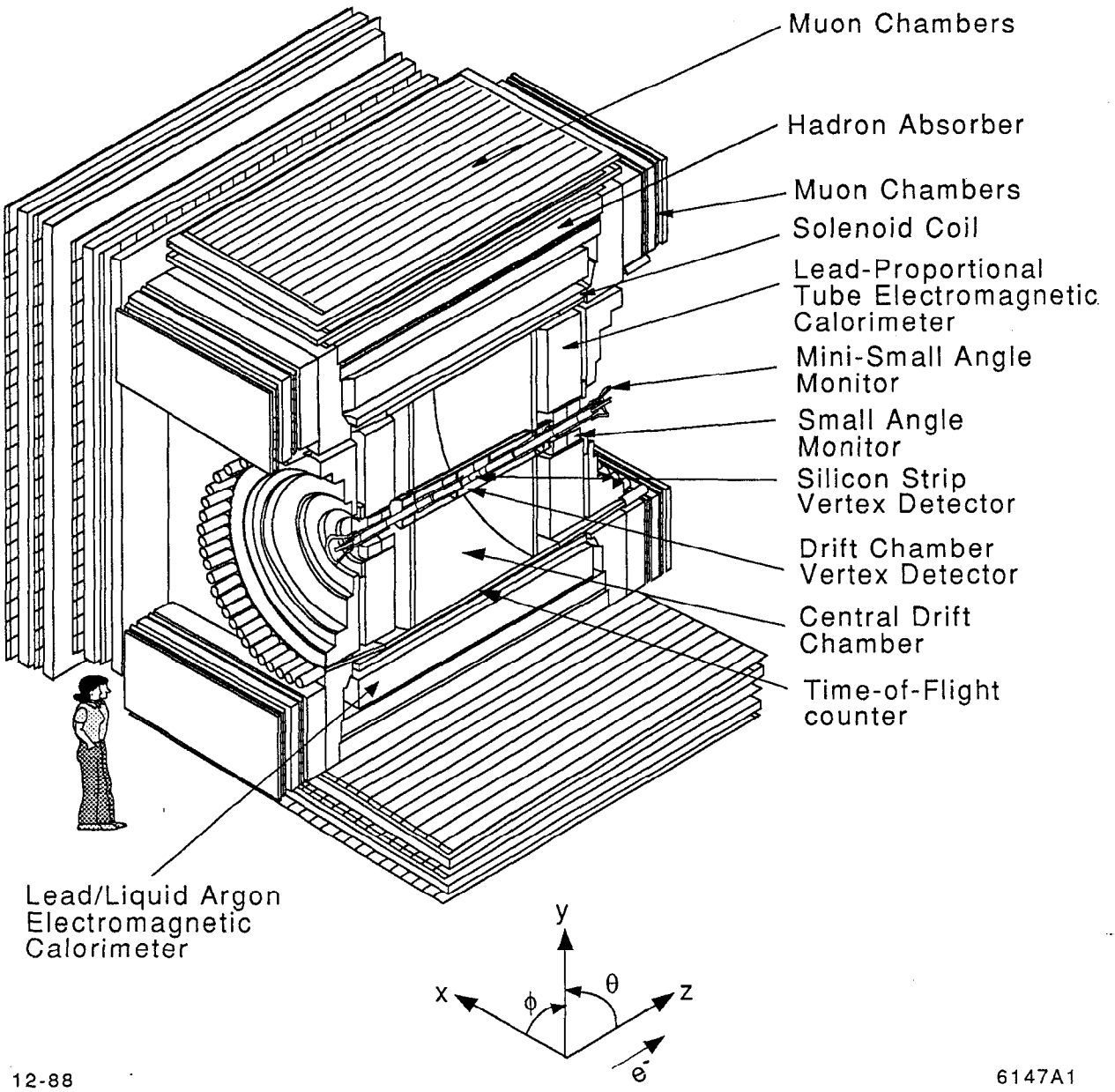

Figure 4: Schematic view of the upgraded Mark II detector. The two vertex detectors were not installed for the data sample in this report.

Table 5: Design parameters for the central drift chamber.

Layer	Radius at center (cm)	Stereo Angle (degrees)		Number of cells
		Wire 1	Wire 6	
1	27.05	0	0	26
2	38.25	3.65	4.07	36
3	48.45	0	0	46
4	59.25	-3.73	-4.00	56
5	69.45	0	0	66
6	80.15	3.76	3.96	76
7	90.35	0	0	86
8	100.95	-3.77	-3.93	96
9	111.15	0	0	106
10	121.65	3.77	3.91	116
11	131.85	0	0	126
12	142.35	-3.78	-3.89	136

evaluation.

3.1 Central Drift Chamber

A new central drift chamber was built for the SLC run to improve the momentum resolution, the two track separation and the pattern recognition. Some charged particle identification capability through dE/dx measurements is also possible.

3.1.1 Drift Chamber Design

The drift chamber design is based on a six sense-wire cell, a shortened version of the jet-chamber configuration [27]. The cells are arranged in twelve concentric cylindrical layers, alternating between wires parallel to the cylinder axis (axial layers) or inclined at approximately $\pm 3.8°$ to the axis to provide stereo information. The

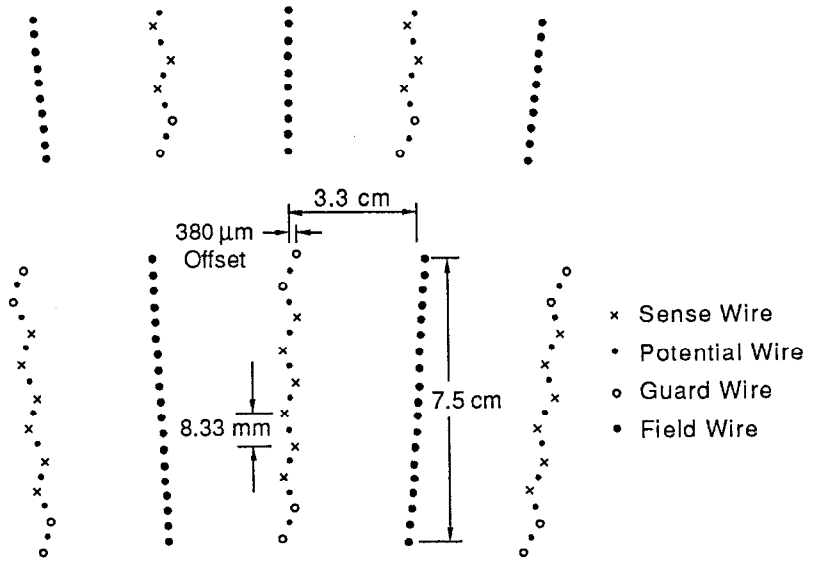

Figure 5: Cell design for the central drift chamber.

inner radius of the drift chamber is 19.2 cm, the outer radius is 151.9 cm and the active length is 2.30 m. The design parameters are given in Table 5.

The detailed cell design is shown in Figure 5. The sense wires (30 μm diameter gold-plated tungsten) are staggered $\pm$380 μm from the cell axis to provide local left-right ambiguity resolution. The electric field is controlled primarily by the voltage on a row of 19 field wires at each edge of the cell. There are also potential wires interspersed with the sense wires and guard wires which help to adjust the electric field and the gains on the sense wires.

The wires are strung between 5.1 mm-thick aluminum endplates which are held apart by a 2 mm-thick beryllium inner cylinder and a 1.27 mm-thick aluminum outer shell. In addition there are eight 2.5 mm by 5.1 mm aluminum ribs attached to the outer shell which provide structural support. The aluminum shell and beryllium cylinder are lined with skins of copper-clad Kapton; a voltage is applied to these skins

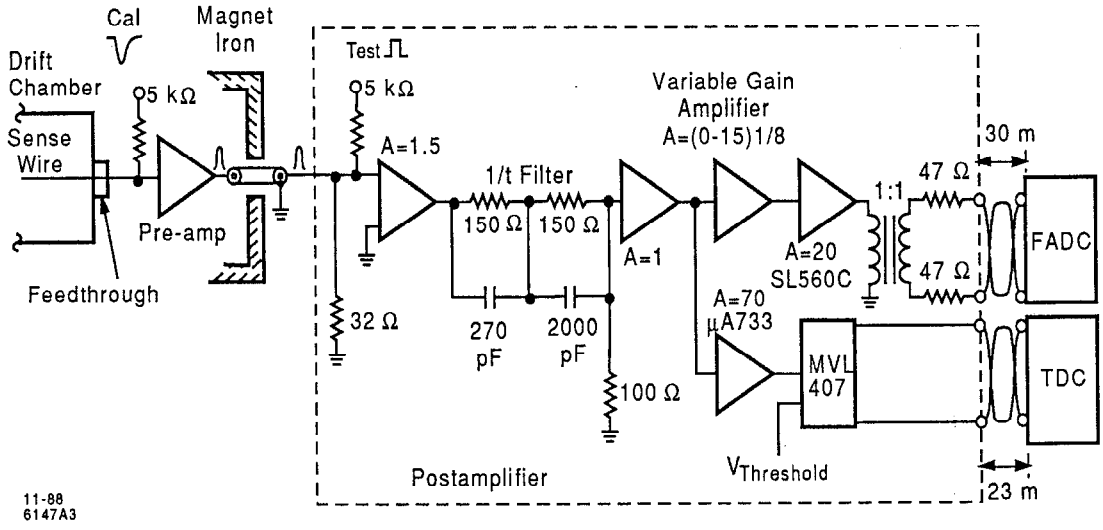

Figure 6: Schematic of the central drift chamber electronics.

to maintain a uniform electric field in the innermost and outermost layers.

The wires in one plane in a cell are located in machined notches in a plastic feedthrough which is pinned to accurately machined holes on the endplate. The average uncertainty in wire location is 35 μm and is primarily due to errors in machining and placement of the feedthroughs and endplates. A more detailed description of the chamber design can be found in reference [28].

3.1.2 Drift Chamber Electronics

The drift chamber signals are amplified in two stages and then digitized. Both a time digitization and a pulse shape digitization (allowing the dE/dx measurement) are made. Figure 6 is a schematic drawing of the drift chamber electronics.

The preamplifier (first stage) boards are mounted directly on the feedthroughs at the chamber face, inside an aluminum RF shield. The circuitry is based on the

Plessey SL560C chip. The second stage of amplification is performed by the 24-channel postamplifiers located in crates mounted on the magnet iron. In addition, these boards shape and split the signal. The timing half of the postamplifier has a gain of 70 and discriminates the pulses using a LeCroy MVL407 comparator. The threshold set for the comparator corresponds to 80 μV at the preamp input. This is equivalent to 4% of the mean pulse height due to a minimum ionizing particle. The gain setting for the pulse height measurement can be varied. More details on the preamplifiers and postamplifiers can be found in reference [29].

At this point, the two sets of signals (timing and pulse shape) are led out approximately 30 m to the electronics house. The drift times are digitized by 96-channel LeCroy 1879 TDCs located in 4 FASTBUS crates. These modules have multi-hit capability and a time bin width of 2 ns. The drift chamber pulses are digitized by SLAC-designed [30] FASTBUS boards. These boards are 16-channel 100 MHz Flash ADCs with 6-bit resolution based on the TRW 1029J7C chip.

The readout of both the TDCs and FADCs is controlled by SLAC Scanner Processors (SSPs) [31], which are programmable FASTBUS modules. One SSP is used in each FASTBUS crate to preprocess (*e.g.* perform zero suppression and pedestal corrections) and format the data. The crate SSPs are read out via cable segments by system SSPs, which buffer the data and interface with the experiment host computer, a VAX 8600. Programs on the host computer correlate the TDC and FADC hits on each wire. The timing and pulse height channels are calibrated separately. For both, the calibration pulse is injected at the input to the preamplifier. The timing calibration measures the time propogation differences for each channel. The pulse height calibration measures a pedestal, gain, and quadratic correction for each channel.

3.1.3 Drift Chamber Operation

A graded high voltage is supplied to the field wires of each cell through a resistor-divider chain. The voltage on a field wire in the center of a cell is typically -4.5 kV, the potential wire and guard wire voltages are typically -1.5 kV and -200 V respectively, and the sense wires are grounded. The copper skins lining the inner and outer cylinders are typically set at -2.5 kV. The drift chamber high voltages and currents are controlled and monitored using an IBM PC.

The chamber gas is a mixture of 89% Ar, 10% CO_2 and 1% CH_4 (HRS gas) and is at a pressure slightly above 1 atmosphere. The above voltages result in a gas gain of approximately 2×10^4 with an electric drift field of 900 V/cm and the typical drift velocity is 52 μm/ns. For the data sample used in this report, the magnetic field was 4.75 kG, giving a Lorentz angle of 18.6°.

3.1.4 Drift Chamber Performance

Tracking Efficiency

The drift chamber tracking program utilizes the multi-sense-wire feature of the cells and forms track segments within cells. These segments are later matched to form tracks through the chamber [32]. The track-finding routine efficiency has been measured at PEP and estimated for SLC using Monte Carlo programs. For low multiplicity events at PEP with tracks which go through all sublayers, the efficiency was measured to be approximately 99%. It has been estimated to be $> 95\%$ for high multiplicity hadronic events at SLC energies. Figure 7 shows the efficiency as a function of $\cos\theta$ for these two classes of events.

Position and Momentum Resolution

The position resolution in the chamber is primarily limited by diffusion in the gas.

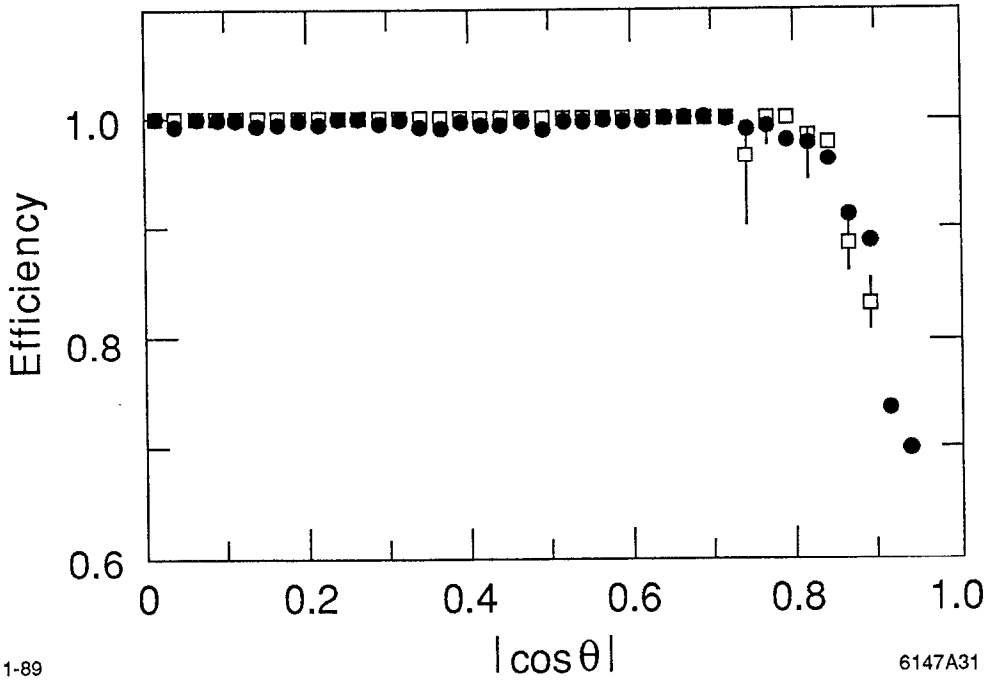

Figure 7: Tracking efficiency for the central drift chamber as a function of cos θ. The hadronic events (boxes) are from a Monte Carlo study; the Bhabha events (points) are from a sample of PEP data.

Calculations show that this effect contributes an error of $\approx$ 150 μm for the longest drift distances. Other errors are $\approx$ 50 μm from the time measurement error in the electronics and $\approx$ 35 μm from wire placement. When a single drift velocity was used for all cells and layers to convert the drift times to positions, the achieved resolution was 185 μm. Fitting velocities for each of 3 drift distance regions in a cell and for different groups of wire layers improved the resolution to $\approx$ 170 μm.

The information from the FADCs can be included in the timing measurement by using the deposited charge to make a "time-slewing" correction. This correction compensates for the change in measured time as a function of pulse height and improves the resolution by a small amount.

Figure 8 shows the resolution versus drift distance with and without the time-slewing correction. However, the major tracking improvement provided by the FADCs is a better double hit separation. Scanning algorithms that use the pulse shape have an efficiency of 80% for separating hits 2.5 mm apart compared to 5 mm if only the TDCs are used.

Using Bhabha scattering events from PEP data in a 4.5 kG field, a momentum resolution of $\sigma(p)/p^2 = 0.46\%$ GeV^{-1} was measured in the central drift chamber for single tracks. The resolution is $\sigma(p)/p^2 = 0.31\%$ GeV^{-1} if the tracks are constrained to originate from a single point (see Figure 9). The multiple scattering contribution to the resolution from the drift chamber itself is 1.4%. This number increases if additional material from, for example, beam diagnostic devices is considered.

Particle Identification

The main purpose of the FADC system is to provide some degree of particle identification, particularly for separating electrons from pions. The charge deposited by a particle traversing the drift chamber is proportional to its energy loss (dE/dx).

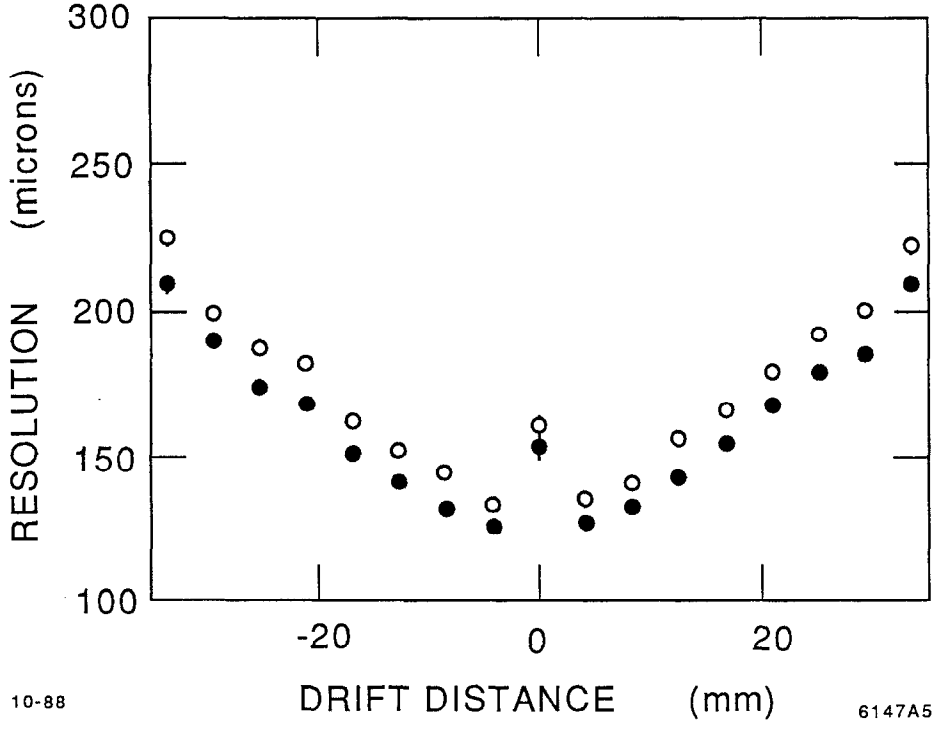

Figure 8: Central drift chamber position resolution versus drift distance, with (closed circles) and without (open circles) the time-slewing correction.

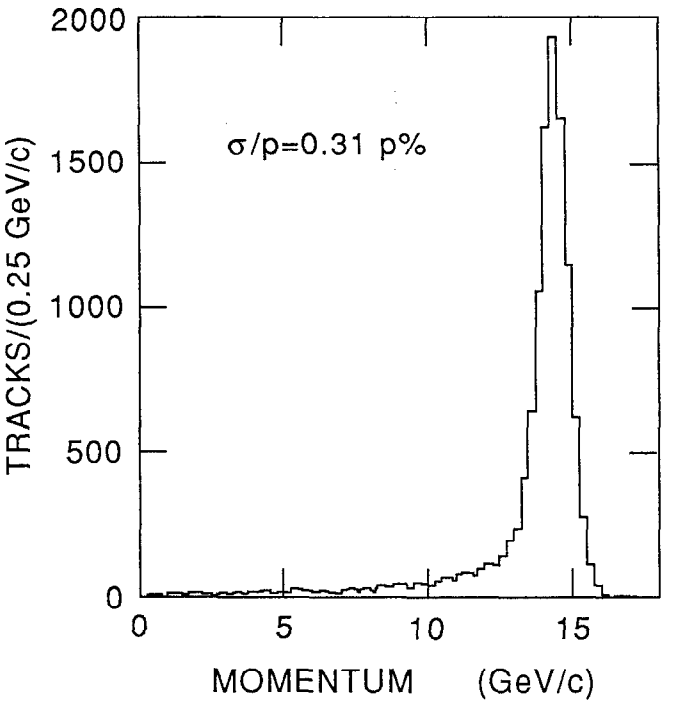

Figure 9: Momentum resolution for the central drift chamber. The tracks are selected from Bhabha events and a constraint that the track originate from a single point is used. The magnetic field was 4.5 kG.

The value of dE/dx coupled with the measured momentum allows a rough determination of the particle mass. For a track travelling the full extent of the central drift chamber, the 72 possible charge measurements would provide an expected dE/dx resolution for minimum-ionizing particles of 6.9% [33]. No particle identification is used in the analysis, so the system will not be discussed here. Reference [34] provides more information.

3.2 Mark II Solenoid

The Mark II solenoid is a conventional cylindrical coil producing a magnetic field of up to 5.0 kG in the center of the detector. Its thickness is 1.3 radiation lengths. The coil consists of twelve aluminum conductors wound in series into four contiguous cylinders. The solenoid is 405 cm long with inner and outer radii of 156 cm and 171 cm respectively. The coil can support a current of 7500 A with a total heat dissipation of 1.8 MW.

The inner radius of the coil is covered by a heat shield which helps to isolate it thermally from the inner detector components. A flow of 40 ℓ per minute of temperature controlled water through the heat shield keeps the temperature within the central drift chamber stable to within a few degrees. The magnetic field inside the cylindrical volume occupied by the drift chamber has been measured and fit to a set of polynomials in coordinates r and z. Within the tracking volume the field is uniform to within 3% while the fit describes the magnetic field with an error of less than 0.1%. The magnetic field used in charged particle tracking is obtained from the fit normalized using the data from two Hall probes positioned at each end of the central drift chamber.

3.3 Liquid Argon Barrel Calorimeter

The central electromagnetic calorimeter of the Mark II is a lead-liquid argon sampling device with strip readout geometry. The calorimeter system consists of 8 independent liquid argon cryostats enclosed in a common vacuum vessel. The system was designed and built as part of the Mark II at SPEAR [35].

3.3.1 Physical Description

Each module measures $1.5 \times 3.8 \times 0.21$ m^3. The modules are arranged in an octagonal barrel outside the magnet coil. Together they cover the polar angle range of $\theta = 47°$ to $133°$ and the full azimuthal angle ϕ except for $3°$ gaps between each pair of modules. The total solid angle coverage is 63.5%.

Each module contains a stack of alternating layers of 2 mm lead sheets and lead strips with the 3 mm gaps between them filled with liquid argon. The lead is strengthened with 6% antimony to minimize sagging. The strips are aligned either perpendicular to the beam axis to measure the polar coordinate θ, parallel to the beam axis to measure the azimuthal coordinate ϕ or at $45°$ relative to the other 2 sets of strips (labeled U) to aid in track reconstruction. Table 6 gives the details for this design.

Spacing is maintained both between strips and between layers by ceramic spacers which contribute an overall dead space of 5%. In order to reduce the number of electronic channels many of the strips are ganged together, both from strip to strip in certain layers and from layer to layer. The ganging results in 6 interleaved readout layers and a total of 326 channels for each module. The ganging scheme is shown in Figure 10. There is an additional pair of 8 mm liquid argon gaps formed by 1.6 mm thick aluminum sheets and strips in front of the lead stack to allow corrections

Table 6: Orientation, width and number of strips per layer in each liquid argon module.

Strip layer	Coordinate measured	number of strips	strip width (cm)
trigger	ϕ	36	3.5
1	ϕ	38	3.5
2	θ	100	3.5
3	U	70	5.4
4	ϕ	38	3.5
5	θ	100	3.5
6	U	70	5.4
7	ϕ	40	3.5
8	θ	100	3.5
9	U	70	5.4
10	ϕ	40	3.5
11	θ	100	3.5
12	θ	100	3.5
13	θ	100	3.5
14	ϕ	40	3.5
15	ϕ	40	3.5
16	ϕ	40	3.5
17	ϕ	40	3.5
18	ϕ	40	3.5

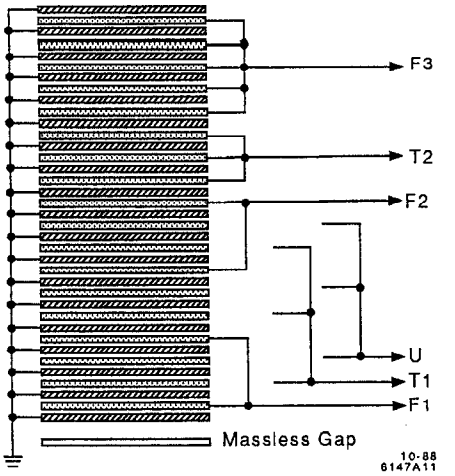

Figure 10: Ganging scheme for the channels in the liquid argon barrel calorimeter.

to measured shower energy for radiative losses in the magnet coil. The strips are oriented in the ϕ direction and there are 36 in each module. Altogether, 1.86 radiation lengths of material precede the lead stack. Together this material and the calorimeter represents 16.0 radiation lengths of material at normal incidence.

3.3.2 Cryogenics System

The total volume of liquid argon in the modules is 6400 ℓ. The argon is not circulated; instead the modules are connected to a common storage vessel through gas phase transfer lines. With an insulating vacuum of 10^{-6} torr surrounding the modules, the major load for the cooling system is the compensation for heat losses in the transfer lines. Temperature is maintained at approximately 85 K using liquid nitrogen refrigeration at the module shells. The system consumes 160 ℓ of liquid nitrogen per hour during normal operation.

3.3.3 Electronics

Charge produced through ionization in the liquid argon drifts to the readout strips in a field of 12 kV/cm. Each readout strip is impedance matched to a TIS75 FET through a small ferrite pot core transformer. The electronic noise is dominated by Johnson noise generated in the conduction channel of the FET and is minimized using a bipolar shaping amplifier [36] with a resolving time of 1.5 μs. The equivalent noise energy in the ganged readout channel varies from 0.3 to 1.5 MeV and is a function of the capacitance of the channel which varies from 0.9 to 8.0 nF. The preamplifiers and shaping amplifiers are mounted on the detector. RF shielding encloses the modules, the amplifiers, and the twisted pair signal cables that run from the amplifiers to the electronics house.

Sample-and-hold modules (SHAMs [37]) follow the output voltage of the amplifiers and are gated to hold at the peak. The charge stored in the SHAMs is measured with 12-bit ADCs incorporated in a microprocessor, BADCs [38]. The BADC in each of the six CAMAC crates performs pedestal subtractions, linear gain corrections, and threshold cuts. The maximum time for digitization and reduction of all data in a CAMAC crate is 6 ms. Thresholds are normally set so that the noise occupancy is about 5%. After ten years of operation, the number of dead channels in the system (due to failing electronics or unrepairable internally shorted strips) is less than 1%.

3.3.4 Performance

The measured energy distribution from Bhabha scattering events at PEP is shown in Figure 11 (the number of Bhabha events in the SLC data is too small to provide a measurement). The resolution is $\sigma/E = 4.6\%$, measured using the width of the distribution at half maximum. However, the distribution is not Gaussian due to

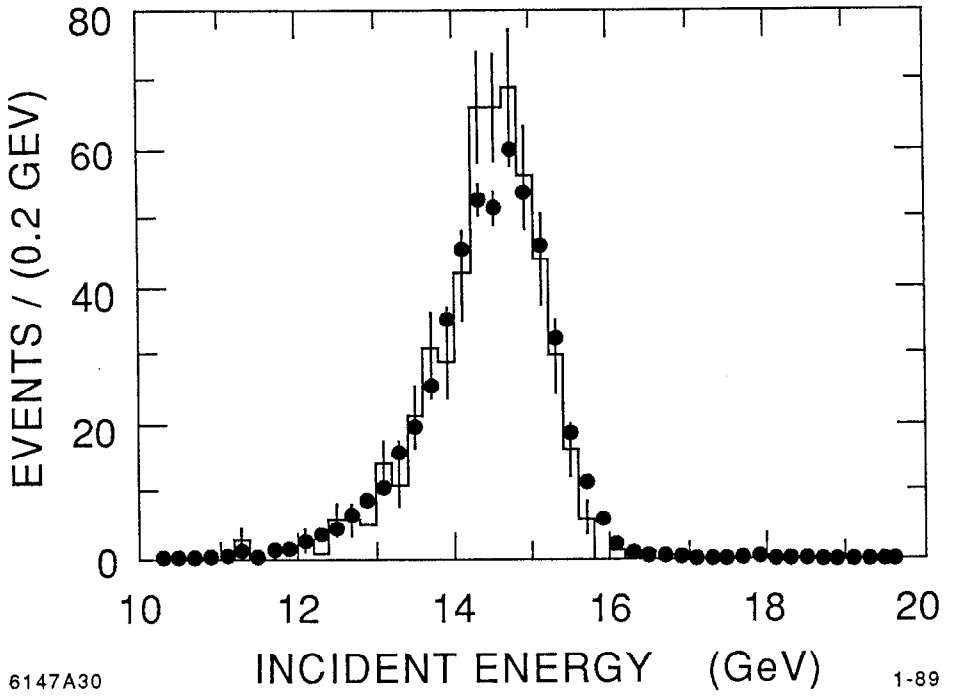

Figure 11: Measured energy distribution for the liquid argon calorimeter from Bhabha scattering events at PEP. The histogram represents Monte Carlo simulation.

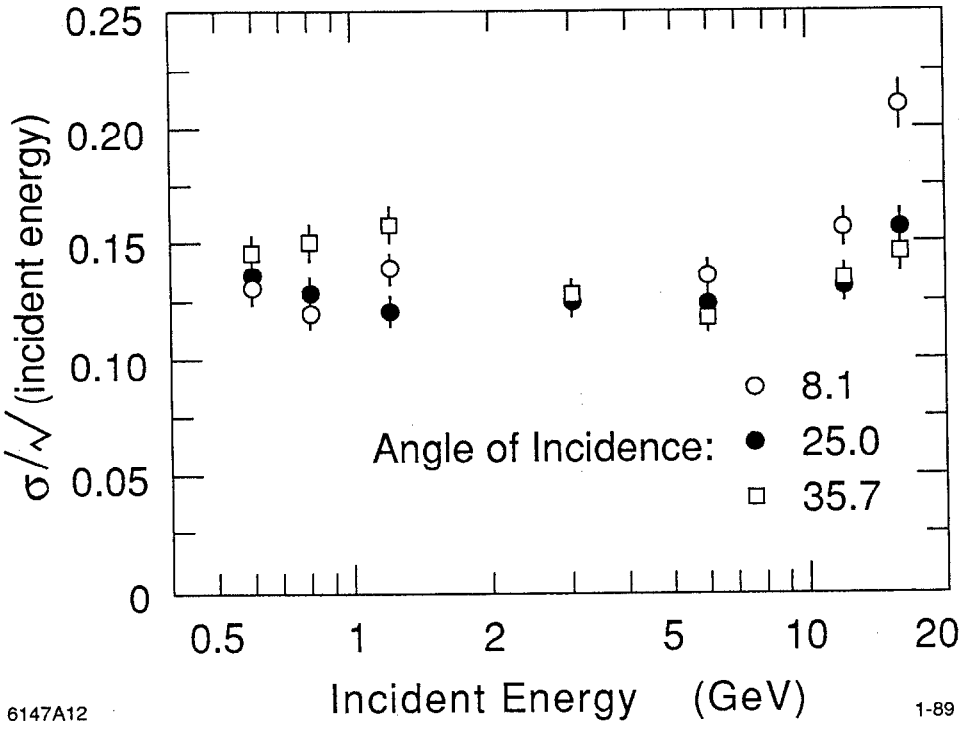

Figure 12: Monte Carlo simulation of the barrel calorimeter energy resolution as a function of energy and angle of incidence.

several reasons. Dead space in the calorimeter active volume creates a low energy tail, the size of which depends on the number of failing channels in the system. Saturation in the readout electronics for the first active layer, used to correct for losses in the coil, further degrades the resolution for high energy electrons in the upgrade data sample. The gain in the amplifiers for the first layer has been reduced so that saturation does not affect running at the SLC. As Figure 11 shows, the Monte Carlo simulation [39], including the effects of dead space and saturation, roughly reproduces the distribution. The energy dependence of the resolution, without saturation, has been studied with the Monte Carlo and is shown in Figure 12. Again, these quantities are difficult to verify with a small data sample. The position resolution measured with the PEP

Bhabha scattering events is 3 mrad in ϕ and 0.8 cm in z and both measurements are consistent with Monte Carlo simulation.

The inclusive electron production analysis [40] performed with data taken before the upgrade provides an example of the electron-hadron separation capability of the barrel calorimeter. In hadronic events, electrons were identified with an efficiency that varied from 78% at 1 GeV/c to 93% at the highest momenta. The hadron misidentification probability was typically 0.5% but could be as large as 3% for tracks of momentum below 2 GeV/c in the core of a jet. A more detailed discussion of the performance of the barrel calorimeter can be found in previous publications [41].

3.4 The End Cap Calorimeter

The end cap calorimeters (ECCs)[42] were added to increase the electromagnetic coverage of the detector. These lead-proportional tube calorimeters are 18 radiation lengths (X_0) thick, and cover the angular region between approximately 15° and 45° in θ from the beam axis. The first layer of the calorimeter is located 1.37 m in z from the interaction point. Together with the liquid argon calorimeter, they provide full electromagnetic calorimetry for 86% of the total solid angle (Figure 13).

3.4.1 Mechanical Design

Each ECC consists of 36 layers of 0.28 cm thick lead (0.5 X_0) followed by a plane of 191 proportional tubes. The tubes are aluminum and have a rectangular cross section of $0.9 \times 1.5\text{cm}^2$. The 191 tubes are glued together with epoxy to form an annular plane with inner and outer radii of 40 cm and 146 cm. A 50 μm diameter Stablohm 800 (nickel-chromium alloy) wire is strung through the center of each tube.

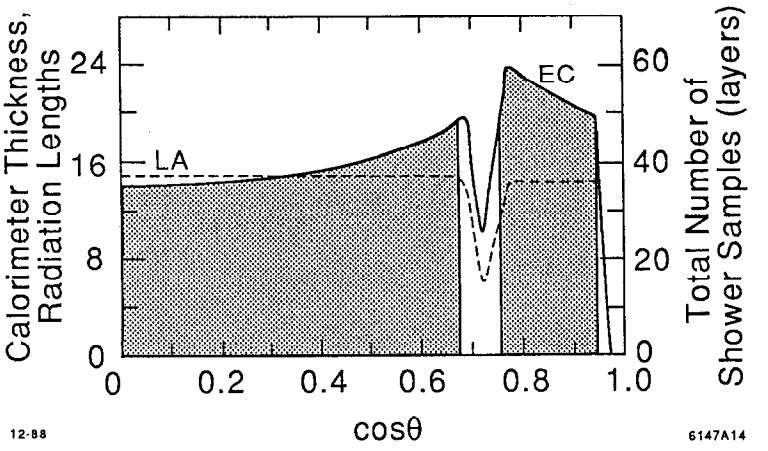

Figure 13: Total calorimeter thickness (in radiation lengths) (solid line) and the number of sampling layers (dotted line) versus $\cos\theta$. The shaded area shows the region used for calculating the solid angle coverage.

Alternating layers of tubes and lead are bonded together with 0.02 cm thick epoxy-saturated fiberglass cloth to a flatness tolerance of 0.06 cm. The first twenty tube planes are oriented alternately in four different directions: vertically (X), horizontally (Y), canted $-45°$ (U), and canted $+45°$ (V). The remaining sixteen layers alternate between X and Y layers.

The gas (HRS gas) flows at slightly above atmospheric pressure through the proportional tubes at a rate of one volume per two days. The outer radius of the ECC consists of sixteen 0.16 cm thick Lexan panels, which are made gas-tight with vinyl tape and epoxy.

To compensate for the variation of the gas gain with gas density, the temperature is measured with thermistors embedded in each ECC and the pressure is measured with transducers on the gas inlets and outlets. The variation of the ECC response is less than 2% after correcting for density changes. This stability is verified by the pulse height spectrum recorded by two small tubes that contain ^{55}Fe sources. These

tubes, which are mounted on the inlet and outlet of the gas system for each ECC, are primarily used to monitor the gas quality.

3.4.2 Electronics

The signals from several tubes are ganged together to reduce the number of electronic channels to 1276 per endcap [43]. Tubes are grouped in depth and in some cases laterally to give ten interleaved measurements of the longitudinal shower development. The ganging follows a projective geometry so that all tubes in a channel lie approximately in a plane containing the interaction point.

The first half of the readout electronics of the ECCs consists of charge-sensitive preamplifiers and shaping amplifiers mounted in electronics crates close to the detector. These are connected to the tube anodes by coaxial cables that carry both high voltage and signals. The second part of the system is a set of SHAM IIs and BADCs [37,38] located in the electronics building. The system is calibrated by injecting a variable amount of charge into the front end of the preamplifiers. During readout, pedestal and gain corrections are applied to the data and a threshold cut is made.

3.4.3 Performance

One of the ECCs was tested in a positron beam and a pion beam prior to installation. Figure 14 shows the response of the ECC to pulses containing between one and five 10 GeV positrons. The five peaks are clearly distinguishable. The beam test data has been used to develop algorithms that reject 99% of isolated pions while retaining 95% of electrons at a momentum of 5 GeV/c.

A study of Bhabha events in the ECCs at PEP [44] gave an energy resolution of $22\%/\sqrt{E}$ (E in GeV). Since the PEP run there has been a substantial decrease in

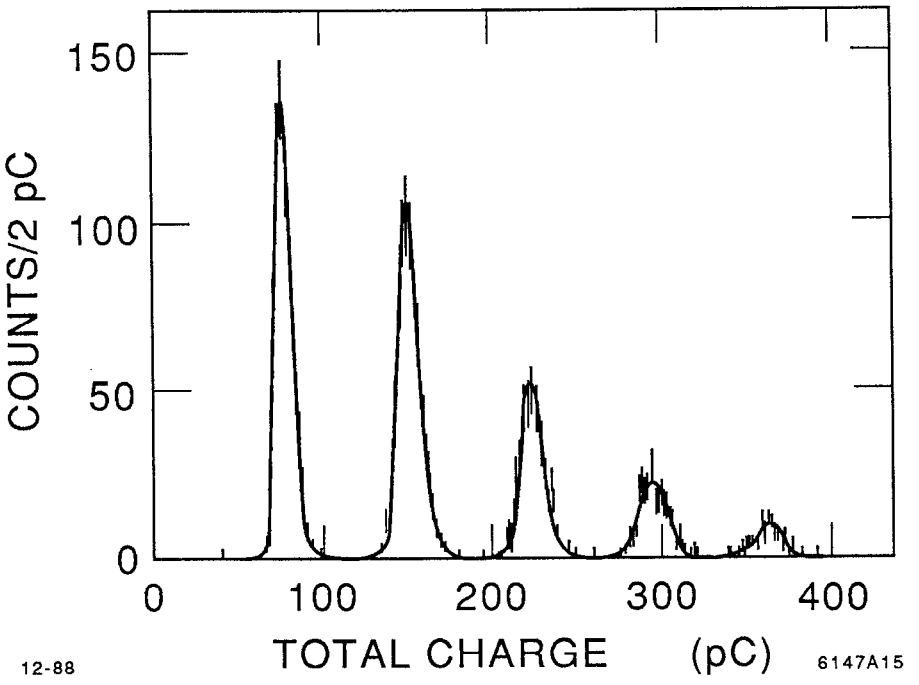

Figure 14: Response of the end cap calorimeter to small numbers (1–5) of 10 GeV positrons.

the number of dead channels and an improvement in the gas tightness of the system, so this resolution is a conservative number for the SLC data. A position resolution of 0.7 cm in both the x and y directions was measured.

3.5 Luminosity Monitors

Two detectors whose main function is to precisely measure the integrated luminosity have been built especially for SLC running. The Small Angle Monitor (SAM) covers the angular range 50 mrad $< \theta <$ 160 mrad, and the Mini-Small Angle Monitor (Mini-SAM) covers 15 mrad $< \theta <$ 25 mrad. Both detectors use small-angle Bhabha scattering to measure luminosity.

3.5.1 Small Angle Monitor

Mechanical Design

The SAM consists of a tracking section with 9 layers of drift tubes and a sampling calorimeter with 6 layers each of lead and proportional tubes (see Figure 15). Each layer of lead is 13.2 mm thick giving a total of 14.3 radiation lengths. There are four SAM modules, two on each side of the interaction point (IP). The distance of the front face of the SAM from the IP is 1.38 m. Pairs of SAM modules are assembled around the beam pipe as is shown in Figure 16. The layers are arranged in 3 different orientations. The tubes in the first layer (Y) are horizontal and the other two layers (U,V) are rotated $\pm 30°$ from Y when looking at the front face of SAM from the IP. For both the tracking and calorimetry layers, the pattern of layer orientation is a series of repeating triplets YUV as seen from the IP.

Both the drift and proportional wire planes are constructed from square aluminum

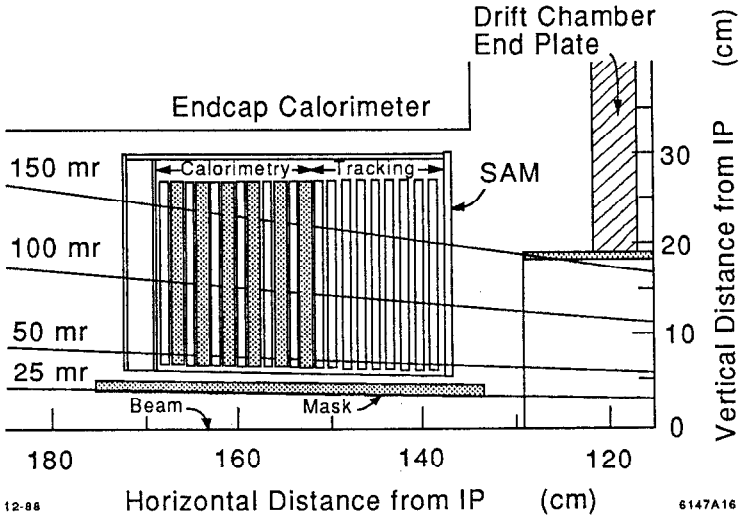

Figure 15: Side view of one of the four hemispherical SAM modules showing its location inside the Mark II detector.

tubes 9.47 mm wide with a wall thickness of 0.25 mm. The sense wire in each tube consists of 38 μm diameter gold-plated tungsten. Positive high voltage is applied to the sense wire with respect to the tube wall which is at ground potential. This voltage is 1800V for the tracking tubes and 1700V for the calorimeter tubes. Each of the four SAM modules contains 30 tubes per layer giving 270 tracking and 180 calorimeter cells per module. All tubes operate with HRS gas. Since the gas gain depends strongly on the density, the temperature and pressure of the gas are monitored by thermistors and transducers mounted on the SAM modules.

Electronics

The electronics for the tracking part of the SAM consists of LeCroy LD604 amplifier/discriminators and TACs [37] that are read out by BADCs [38]. The calorimeter part is instrumented with custom-designed amplifiers and the signals are stored in SHAMs [37] which are also read out by BADCs.

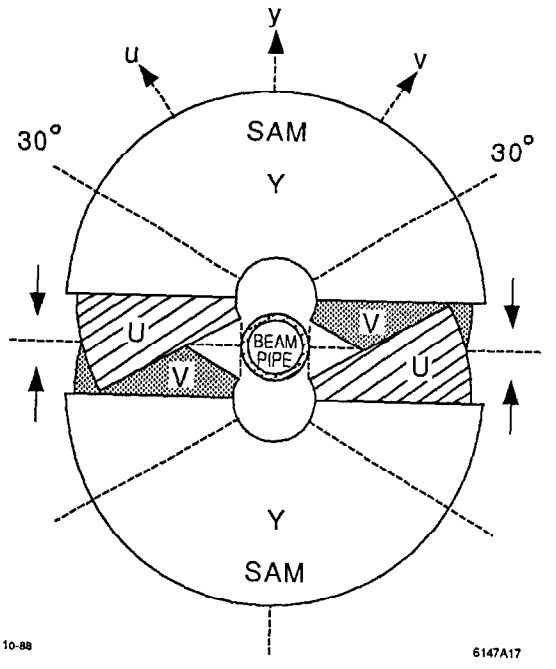

Figure 16: View of two SAM modules as seen from the interaction point. The figure shows the axes for the orientation of drift and proportional tubes as well as the method of assembly around the beam pipe.

Calibration pulses are injected at the input to the amplifier with variable time delays and constant pulse height for TACs and with constant time delay and variable pulse heights for SHAMs. The resulting signals are fit linearly or quadratically to extract the calibration constants which are then stored in the BADCs for subsequent application to incoming data.

Performance

One of the four identical SAM modules was tested in a beam of positrons at 5, 10 and 15 GeV. The measured tracking resolution was 250 μm, which yields an intrinsic angular resolution for Bhabha tracks of 0.2 mrad assuming the SLC interaction point is known. The measured energy resolution in the range 5-15 GeV can be parametrized by $\sigma/E = 45\%/\sqrt{E}$ (E in GeV) for showers near the center of the SAM active area. The resolution worsens somewhat at the edges because of radial shower leakage. Longitudinal shower leakage increases from 9% at 5 GeV to about 22% at 50 GeV, and fluctuations in this leakage degrade the energy resolution. The position resolution for locating showers with just the calorimeter section of the SAM is 3 mm. This number is used for matching tracks with showers and also represents the precision with which photons entering the SAM can be located. The SAM Bhabha rate is estimated to be roughly 20% higher than the visible Z^0 rate. The experimental systematic error on the luminosity measurement was $\approx 2\%$.

3.5.2 Mini-Small Angle Monitor

Mechanical Design

The Mini-SAM surrounds the beam pipe 2.05 m on either side of the IP. It is composed of six layers of 0.64 cm thick scintillator interleaved with 0.79 cm-thick tungsten slabs providing 15 radiation lengths in total thickness and resulting in an expected

energy resolution of $35\%/\sqrt{E}$ (E in GeV). The first scintillator layer is preceded by 2 layers of tungsten (4.5 radiation lengths) as a pre-radiator. The layers are divided into four equal azimuthal segments, each read out with a Hamamatsu R2490 photomultiplier tube viewing a wavelength shifter bar running the length of each azimuthal segment. Angular acceptance windows are sharply defined by 5.08 cm thick conical tungsten masks (15 radiation lengths). These masks are asymmetric; reasons for this include allowing for motion of the interaction point without reducing acceptance, and allowing for Monte Carlo/data disagreement at small acollinearity angles. The angular acceptance is 15.2 mrad $< \theta <$ 25.0 mrad on one side of the IP, and 16.2 mrad $< \theta <$ 24.5 mrad on the other side.

Electronics

The Mini-SAM readout electronics use a BADC – SHAM IV combination similar to that used by the liquid argon barrel and endcap calorimeter systems. The system also emplys TACs [37] to provide timing information for the signals. The Mini-SAM is read out on every trigger to monitor noise. Signals are also sent from the Mini-SAM to the trigger logic to provide an additional Bhabha trigger.

Performance

The Mini-SAM as installed was not tested in a beam; however, a very similar prototype was placed in a 10 GeV e^- test beam, and these tests confirmed EGS [39] shower studies of both the shower profile and the predicted performance of the tungsten aperture masks. A test of the integrity of the Mini-SAM has been made using cosmic rays. The observed cosmic ray signals were used to set an approximate energy scale for the device.

To measure luminosity, small angle Bhabha pairs must be detected above a potentially large machine background. All events which had $>\sim$ 20 GeV deposited energy

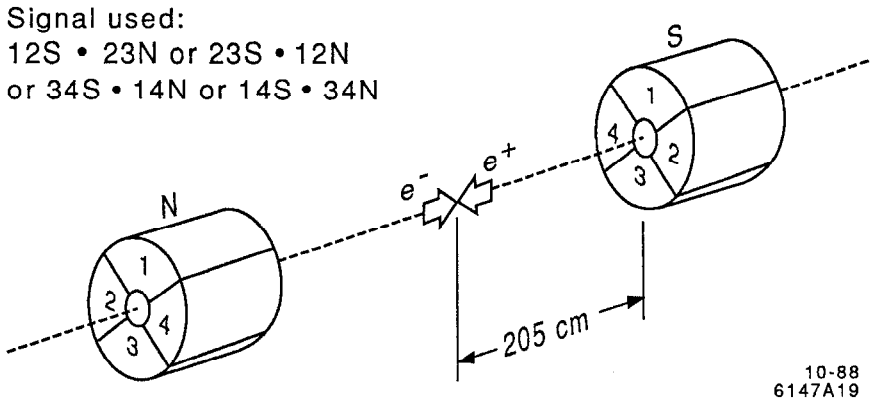

Figure 17: Geometry of the Mini-SAM. As an example, in the 'Signal Used' definition, 12S means the signal sum of quadrants 1 and 2 being over a Bhabha threshold in the south monitor.

in both sides qualified as a Mini-SAM trigger. A Bhabha pair is defined by back-to-back coincidences of discriminated signal sums of adjacent azimuthal segments as shown in Figure 17. The rate of accidentals is measured by forming coincidences between azimuthal segments which are not back-to-back. Other cuts are made off-line (*e.g.* requiring the timing to be consistent with an e^+ or e^- entering the front side of the segment) to obtain the corrected luminosity. The tungsten masks defining the angular acceptance result in a Mini-SAM Bhabha rate of approximately eight times the total estimated visible Z^0 rate at $\sqrt{s} = M_Z$.

3.6 Trigger

The trigger used for running at the SLC combines a modification of the trigger used at PEP with new FASTBUS based logic. The SLC beam crossing rate was 10, 30 or 60 Hz for the sample collected for this report. Since this allowed sufficient time to run the trigger logic on every beam crossing, the beam crossing signal supplied by

the accelerator provided the primary trigger. The interface between the trigger logic and the host VAX is provided via CAMAC by the Master Interrupt Controller (MIC) module. Details of the trigger combination for the data sample collected are given in section 4.1.

3.6.1 Data Trigger

There are three components of the normal data trigger. They use information from the central drift chamber, electromagnetic calorimeters and small-angle monitors. Each component operates independently and provides a degree of redundancy to assist in monitoring the performance of the other components. This redundancy is also used to measure their relative triggering efficiencies.

Charged Particle Trigger

The charged particle trigger uses a fast track-finding processor [45,46] to count the number of charged tracks traversing the drift chamber. Pattern recognition can be done with up to 12 detector layers; for this data sample, the twelve layers of the central drift chamber were used. No information about the z-coordinate is used. This design requires approximately 60 μs to count the charged tracks.

A drift chamber cell is considered "hit" when at least four of the six sense wires in the cell have signals detected by the TDCs. (The number of wires which determine a hit is programmable.) This requirement is a powerful means of rejecting backgrounds which do not produce track segments. Requiring a track to traverse more than half a cell produces a geometrical inefficiency of less than 0.5% for tracks of $p_t \sim 1$ GeV/c.

The pattern of hits in each layer is loaded into a shift register and transferred serially into special hardware curve-finding or "curvature" modules as shown in Figure 18. Each curvature module is programmed to identify patterns of hits falling

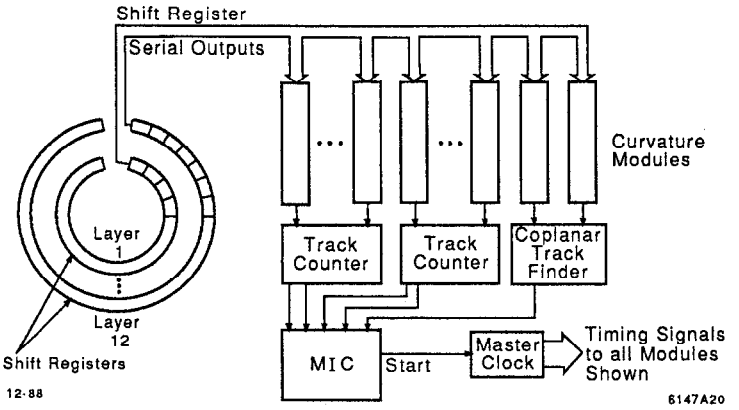

Figure 18: Block diagram of the charged particle trigger

within a specific range of radii of curvature called a road. These modules can also be programmed to require any pattern of layers to define a valid track.

Track counters are used to record the total number of tracks found as well as the azimuth of each track. All tracks found by curvature modules within $\sim 10°$ in azimuth of each other are counted as a single track. The total number of tracks found is encoded into two bits which are passed to the MIC for the trigger decision.

Finally, a coplanar track finder is used to look specifically for back-to-back tracks. It uses two curvature modules to estimate the azimuth of tracks, and returns a bit to the MIC when a pair of tracks are found that are coplanar to within $\sim 11°$.

Calorimeter Energy Trigger

The calorimeter energy trigger uses a table of constants stored in a memory module to find events with topologies of interest. The event topology is defined by thresholds placed on the energy deposited in the liquid argon, endcap and SAM calorimeters, and in small-angle counters.

A programmable Memory Logic Module (MLM) encodes 32 input bits into two output bits which are returned to the MIC; this requires a few hundred nanoseconds.

The MLM uses information from the SAM and Mini-SAM to form a low-angle Bhabha trigger for luminosity monitoring, while calorimeter information is used for the Total Energy Deposition (TED) trigger. The TED trigger uses groups of eight adjacent channels (strips in the liquid argon calorimeter; proportional tubes in the endcap) which are summed at the detector. The sum representing one LA module is compared with a threshold voltage by a strobed discriminator [47]. The sum for an endcap is fed into two discriminators with different thresholds. The determination of these thresholds is ultimately limited by the maximum trigger rate permitted by the data acquisition system.

SSP-based Software Trigger(SST)

The SST was more recently designed to duplicate the capability of the TED trigger and, in addition, to provide new software flexibility for improving both its noise sensitivity and pattern recognition characteristics. The redundancy available to the two triggers does, in addition, provide an important cross check for calorimeter triggering. A SLAC Scanner Processor (SSP) is the component of the SST which processes the calorimetric data in a much more flexible manner than the TED trigger. Copies of the LA and EC trigger sums are made by summing/buffer boards which are then digitized by LeCroy 1885N FASTBUS ADCs. In one pass the SSP reads out the ADCs and defines "hits" based on three software thresholds. Trigger algorithms then find calorimetric "towers" (clusters of energy which point to the IP) by using the hits to index a table of pre-calculated patterns. (The complexity of the algorithm is constrained only by the time available between beam crossings.) Only the energies of the channels contributing to a tower are summed, therefore the SST eliminates noise from other channels in the modules. More details on the SST system may be found in reference [48]. For most of the data-taking run, the single tower energy threshold

was 2.2 GeV for the LA system and 3.3 GeV for the endcaps.

In addition to the calorimeters, the SST reads out noise monitors through its ADCs. There are 48 ionization chambers in the last section of the SLC beamline, and 16 proportional tubes along the beamline in the experimental hall (and inside the Mark II). An increase in the signals from these monitors is indicative of various accelerator-related problems such as klystron tube and magnet failures or mis-steering of the beams.

3.6.2 Cosmic Ray Trigger

A cosmic ray trigger is needed for debugging and performance evaulation of individual detector components. Cosmic rays are defined using the normal charged particle trigger system in conjunction with a signal from the TOF system to provide an absolute time measurement required by the charged trigger electronics and drift chamber reconstruction software. Cosmic ray data also form an important check of the charged particle trigger performance.

3.6.3 Random Trigger

To monitor the accelerator backgrounds, a random trigger was developed. Pre-scaled to provide a low percentage of the triggers, the events which have only the random trigger are very useful in estimating the energy deposition in the detector when no annihilation occurred. See section 4.4.2 for details of the use of these events.

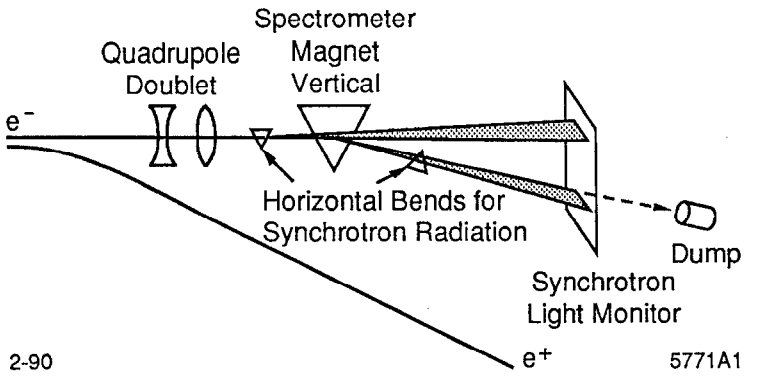

Figure 19: Conceptual design of the extraction line spectrometer (ELS) system.

3.7 The Extraction Line Spectrometer

In order to determine the center-of-mass energy (E_{cm}) at the SLC interaction point (IP), precise measurements of the beam energies (E_{beam}) for both the e^- and e^+ beams are essential. To meet the resolution goal of $\frac{\sigma_{E_{cm}}}{E_{cm}} < 0.05\%$, precision spectrometers were installed [49] in the SLC extraction lines, 150 m downstream of the IP in both beam lines.

3.7.1 Spectrometer Description

A conceptual design of the extraction line is shown in Figure 19. In the line, the $e^{\pm}$ bunch travels through a string of three dipole magnets (B31, B32, and B33). Magnet B32 is a well measured spectrometer magnet (set at $\int Bdl = 30.5$ kG $\cdot$ m when E_{beam} is 50 GeV) which bends the beam by an amount proportional to $\int Bdl/E_{beam}$. Magnets B31 and B33 bend the beam perpendicular to the bend direction of B32 and cause the beam to emit two 5 cm wide swaths of synchrotron radiation. Synchrotron light detectors located at the beam focal point (approximately 15 m from B32) measure the distance between these swaths (approximately 27 cm) and thus the angle through

which the beam has been bent by magnet B32. Combining this information with the strength of the magnet allows a determination of the energy of the beam. Analysis of the widths of the synchrotron stripes yields the energy spread of the beam.

3.7.2 Magnetic Field Monitoring

Two high precision, absolute methods were used to make a determination of the magnetic strength of the B32 magnets before their installation in the extraction line. The first measured $\int Bdl$ directly by moving NMR probes along the length of the magnet, measuring B and dl for each step. In the second method, $\int Bdl$ was measured by monitoring the voltage induced on a moving loop of wire. These methods are described in detail elsewhere [50]. The techniques agreed to better than 0.008%.

The absolute measurements were used to simultaneously calibrate three online methods of determining the spectrometer strength: a flip coil, NMR probes, and current monitors. A cross section of the magnet with these devices installed in the gap is shown in Figure 20. Agreement between the flip coil and NMR probes was better than 0.01%.

3.7.3 Detection of Synchrotron Radiation

The bend magnets cause the beam to emit intense swaths of synchrotron radiation with a maximum energy of approximately 3.0 MeV. An energy spread of 0.2% in the bunches causes the stripe from B33 to be dispersed by about 540 μm at the detector plane. Two independent detectors have been built to detect the separation and width of the two synchrotron swaths: a Phosphorescent Screen Monitor (PSM) (Figure 21) and a Wire Imaging Synchrotron Radiation Detector (WISRD) which was not used during this run.

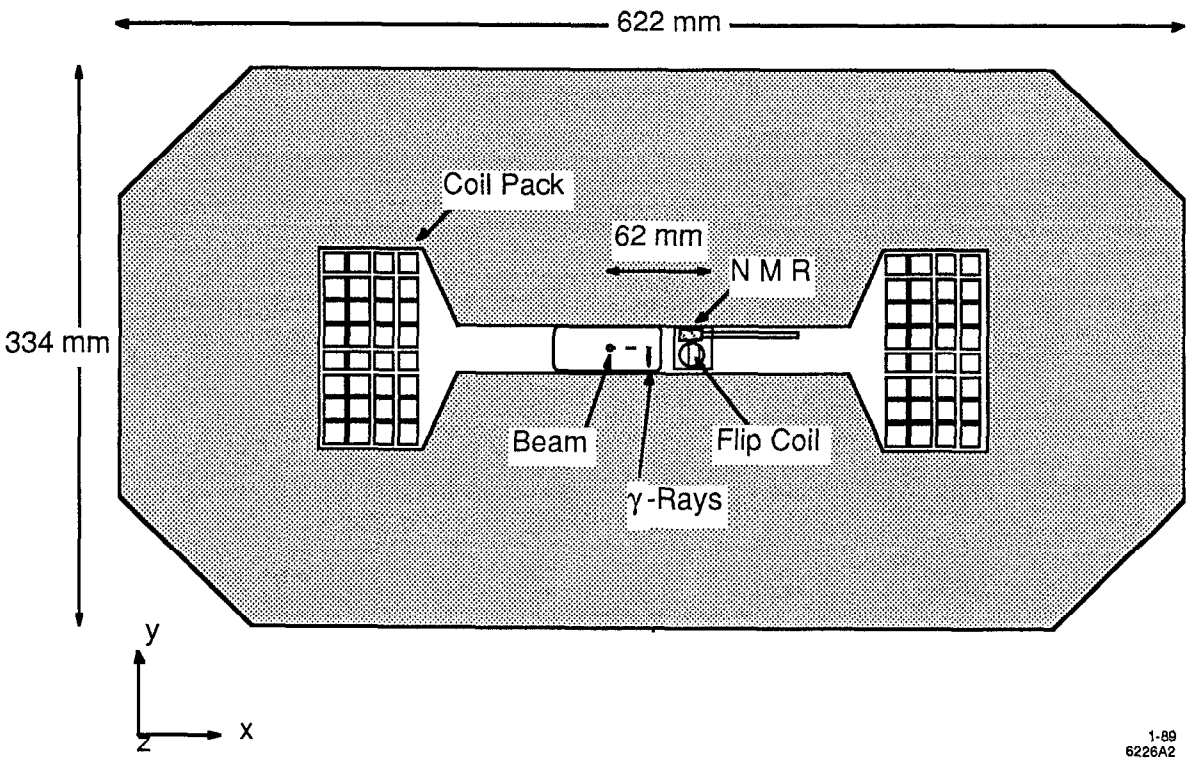

Figure 20: Cross section of B32 magnets showing locations of magnetic strength measuring devices for the ELS.

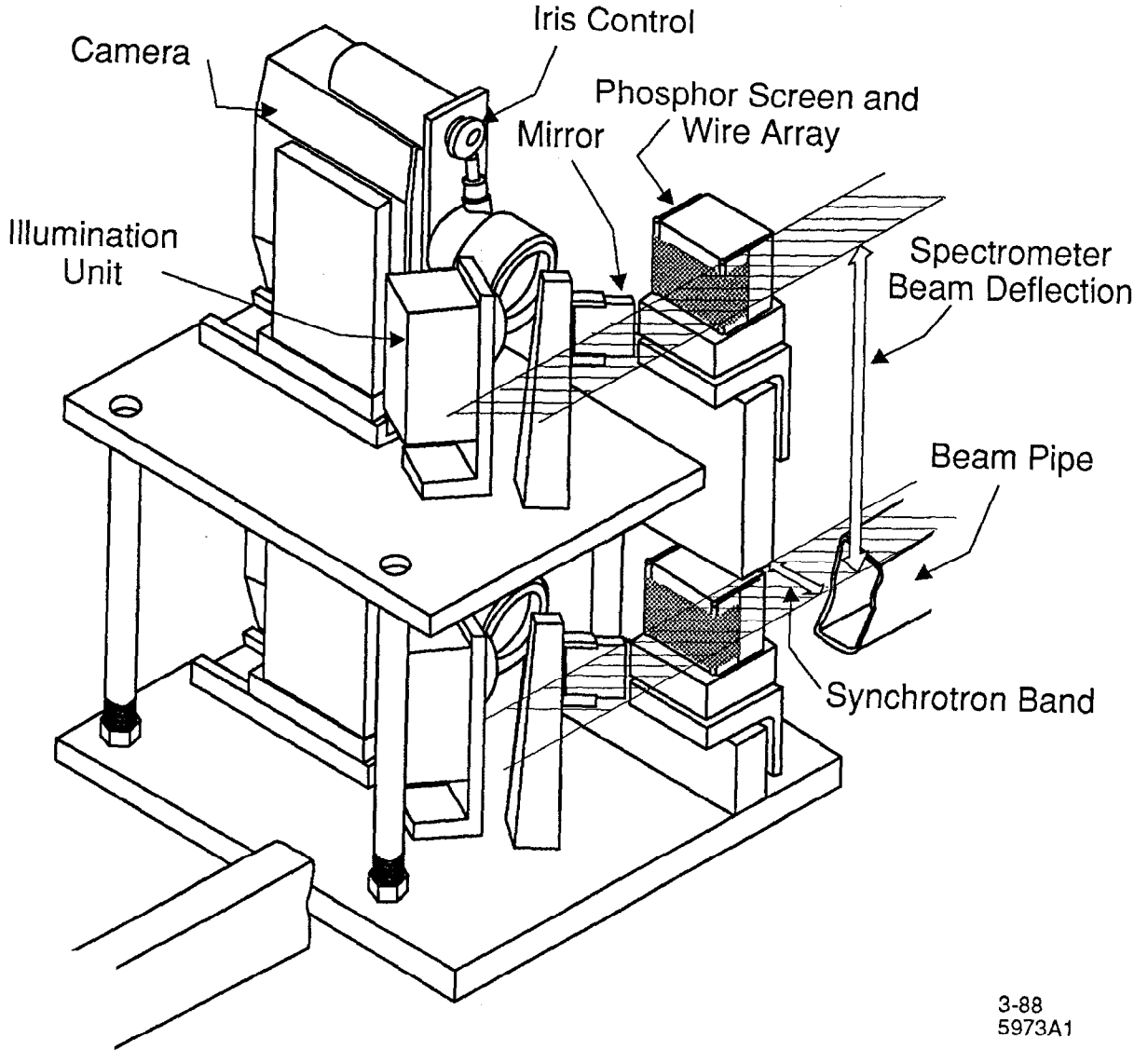

Figure 21: Schematic view of the Phosphorescent Screen Monitor (PSM).

The PSM consists of two identical target and camera systems to monitor both stripes simultaneously. An Invar [51] support structure holds both targets and fixes the distance between them. Each target consists of an array of 100 μm diameter fiducial wires with center-to-center spacing of 500 μm and a phosphorescent screen which emits light where struck by the synchrotron beam [52]. The individual wires and the spacing between the two arrays were measured on precision optical comparators to an accuracy of better than 10 μm. A camera system records both the fiducial wires and the synchrotron stripe which runs parallel to them. The video frame is digitized and compressed by a signal averager into a one dimensional array (perpendicular to the wire direction) before readout. Ultimate system resolution has been measured to be better than 25 μm and readout rates up to SLC design repetition rate (180 Hz) are possible.

3.7.4 Performance

In addition to the previously described errors, there are other contributions to the error on measuring E_{beam}. These contributions include: the survey of distance and misalignments between B32 and the detectors, and misalignments between bend magnets. Combining these contributions in quadrature yields an estimated total error on E_{beam} of 15 MeV. However, knowledge of the average energy of the beam bunch does not necessarily determine the luminosity weighted E_{cm} at the IP. Complete understanding of correlations between particle position and energy in the two colliding bunches is essential to limit the systematic error on the energy measurement. An absolute accuracy of 35 MeV on $E_{e^\pm}$ has been achieved.

3.8 Data Aquisition System

Data acquisition for the Mark II detector is performed by a system of software and hardware elements. The software consists of a number of independent processes running on the host VAX 8600 under the control of the VMS operating system. Each process performs a primary function and communicates with the other processes via shared memory (global) variables, shared instructions and a form of interprocess communication known as event flags. These functions include: reading CAMAC data; reading FASTBUS data; merging of raw data with results from on-line event tagging; tape logging of data records; disk logging of tagged data records; monitoring of detector performance, electronics and environmental status; on-line analysis and histogramming; and operator control of the experiment.

All data from the detector are channeled into the VAX through either the CAMAC or FASTBUS interfaces. The amount of data read per event varies with the event topology. A Z^0 decaying into 20 charged particles will typically result in approximately 50 kbytes of data.

The CAMAC interface is a UNIBUS-based microprocessor system called the VAX CAMAC channel or VCC [53]. This system is capable of transferring 24 bits of data every 2 μs. Generally, however, only the least significant 16 bits are used resulting in a transfer rate of 1 Mbyte/s. The VCC operates a parallel branch serving two system crates [54]. These system crates contain a total of 11 branch drivers which connect with the 44 data acquisition crates. Event triggers are generated within the CAMAC system and are posted as AST (Asynchronous System Trap) interrupts on the VAX. CAMAC event acquisition consists of multiple VAX reads of individual BADC memories and other general instrumentation modules.

The FASTBUS system interface consists of two parts. The first part is a DEC

DR-780 32-bit parallel port which connects the VAX SBI (Synchronous Backplane Interconnect) with a DDI (DR-32 Device Interconnect) cable. This DDI cable connects with another interface [55] which provides access to a FASTBUS crate segment through a simple buffer module, BAFFO (see Figure 22). The combined interface supports interrupt messages and block transfer data rates of approximately 5.5 Mbytes/s between the VAX and an SSP. Two FASTBUS crates running in parallel serve as system crates. One system crate contains five system SSP modules which in turn control each of five FASTBUS cable segments connected to the 25 remote data acquisition crates [56]. Each remote crate contains a single SSP acting as an intelligent crate controller and data processor, along with the data acquisition modules. The second system crate contains a pair of SSPs managing a sixth cable segment used for a future project involving online data processing. Event acquisition begins with remote crate SSPs performing local data readout and processing, then reporting to the appropriate system SSP. The master system SSP acts as an event builder, collecting the entire FASTBUS component of an event into its own local memory before interrupting the VAX. In this way, the FASTBUS system is able to buffer several events before being read out. The VAX then performs a single block read from the master system SSP.

Event acquisition proceeds in the following way. A signal is generated at every beam crossing (*e.g.* 8.3 ms at 120 Hz). This signal starts the trigger logic (see previous section) and BADC processing which requires approximately 8 ms. Note that no dead time is introduced as a result of running the trigger logic for every beam crossing. If a trigger has been received, the VAX reads data from the entire CAMAC system and awaits a signal from the master system SSP that the FASTBUS system is ready to accept the next event. When the signal is received the trigger is reset. FASTBUS data is subsequently read into the VAX, combined with the CAMAC data and a

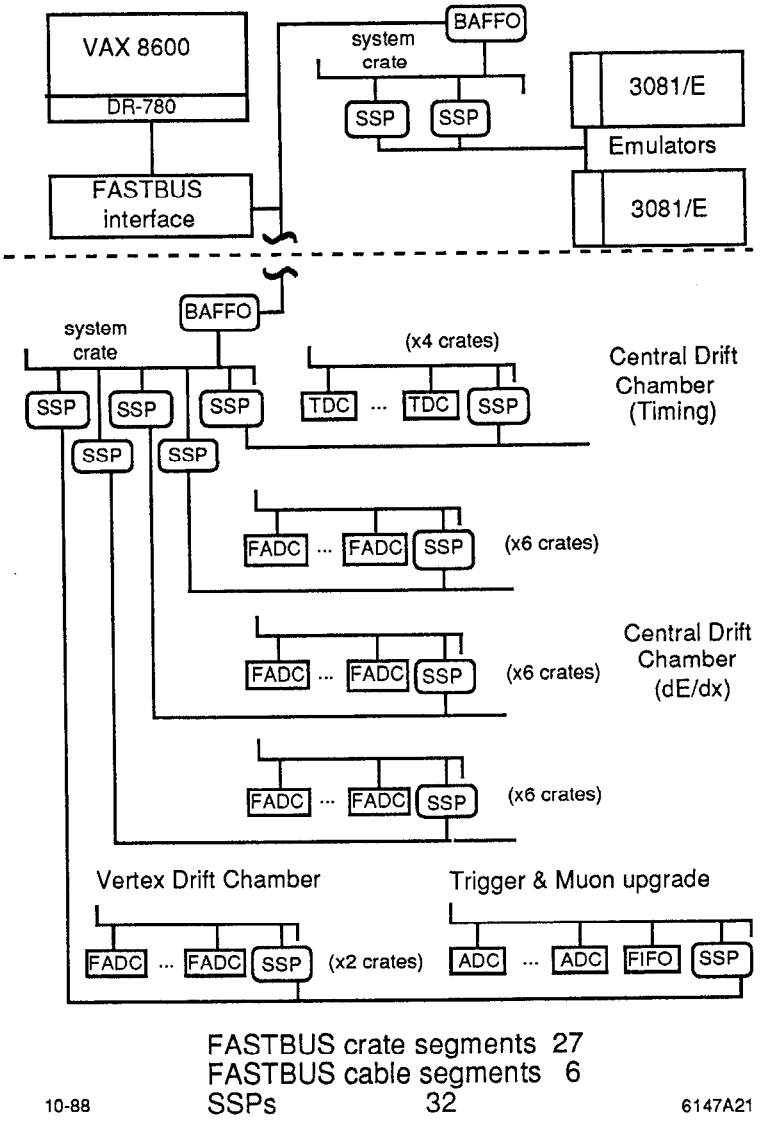

Figure 22: FASTBUS architecture for the Mark II data aquisition system.

simple event tagging algorithm executed. The event is then placed into a global buffer where consumer processes, such as the on-line analysis program, sample the complete events. The tape logging process is the final consumer of all events and, after logging is completed, removes the event from the buffer.

Chapter 4

Event selection

The event selection goal for this analysis was to produce a sample of well-measured hadronic events. The Monte Carlo (MC) simulation of the detector should match the data well (so that corrections can be made for the effects of the detector) and it should be ensured that most of the information about the event is measured. The following sections describe the data sample and the cuts made on the data to further that goal.

4.1 Initial Data Sample

As described in Chapter 3, there are several main triggers for the detector. For most of the time when this data set was collected (April - October 1989), the trigger was a logical OR of the following event characteristics: at least 2 charged tracks, one electromagnetic shower of greater than 3.3 GeV (2.2 GeV) for the barrel (endcap) calorimeter, a trigger from one of the luminosity monitors, a random beam crossing, or cosmic ray events. The efficiency for recording a hadronic Z event was estimated from MC simulations to be $> 99\%$. In total, more than 4.5 million triggers were

recorded.

These events were passed through a simple filter and then written out as the Data Summary Tapes (DSTs). The filter required that at least two tracks originate from a common vertex defined as a cylinder with radius 0.015 m and half-length along the beam axis of 0.03 m. The center of the cylinder must have been located along the beam line and within ± 0.50 m in z from the IP. The total luminosity measured was 19.7 nb^{-1} using the SAM and Mini-SAM luminosity monitors (see section 3.5) [10].

4.2 Charged Track and Neutral Shower Cuts

4.2.1 Charged Track Cuts

The charged tracks in the events were reconstructed using the information from the central drift chamber. Segments were formed from the hits on the 6 wires in each cell. The segments throughout the chamber were then matched if they fell on the arc of a circle. The tracking finding program made several iterations to find the best assignment of hits to tracks. The track fitting program used these assignments to determine the track parameters and their errors. After all of the single tracks were reconstructed, they were refit with the assumption that all came from a common vertex within the specified beam interaction region.

Cuts were initiated by requiring that the tracks originate near to the measured e^+e^- IP. A cylinder was defined with radius 0.01 m and half-length 0.03 m, aligned along the beam direction and centered at the IP. The track origins were restricted to be within the cylinder. Tracks that come from secondary interactions with detector material were therefore mostly avoided. The single track reconstruction yielded the best measurement of the distance of closest approach to the primary vertex. However,

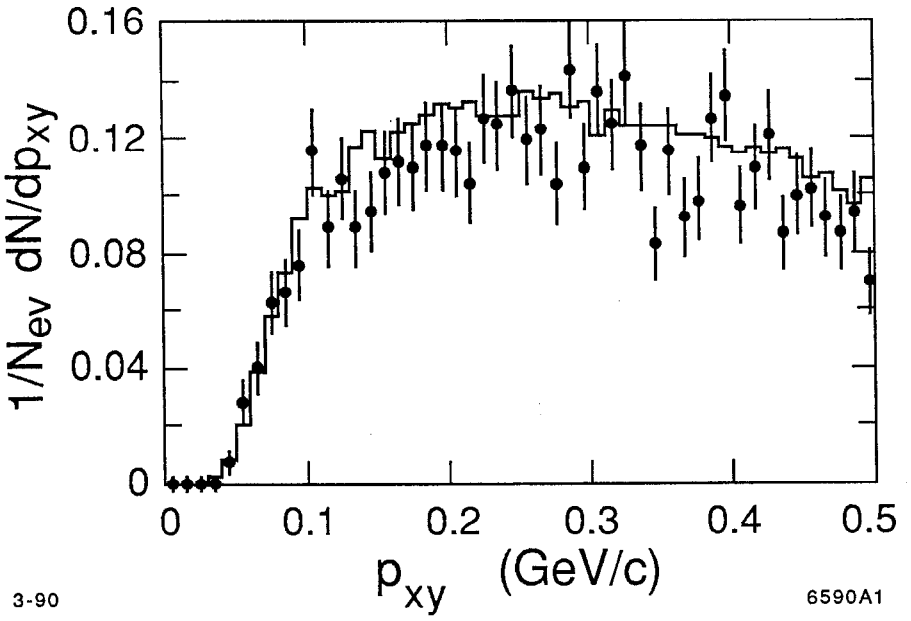

Figure 23: The distribution of transverse momentum values for data (points) and for the MC simulation (histogram). The areas are normalized to the number of events.

studies showed that the vertex-constrained measurement mentioned above gave a more accurate representation of the particles' momenta for values greater than 1 GeV/c. Therefore all subsequent cuts and analyses used the vertex-constrained value.

It was necessary to ensure that the track had a large enough momentum so that a) it did not loop in a full circle under the effect of the magnetic field and b) the efficiency for finding tracks was understood. A particle with momentum perpendicular to the beam axis greater than 110 MeV/c will exit the chamber before curling up on itself. However, as can be seen in Figure 23, the Monte Carlo (MC) with detector simulation overestimates the number of tracks we should find until approximately 300 MeV/c. Therefore a cut was made at this value.

As a track leaves the drift chamber at close angles to the beam pipe, it intercepts less than the maximum 12 layers of wires and less information is gathered. Table 7

Table 7: The outermost radius and corresponding cos θ value for each superlayer.

Layer	Radius of wire 6 (m)	cosθ
1	0.291	0.964
2	0.403	0.934
3	0.505	0.901
4	0.613	0.864
5	0.715	0.827
6	0.822	0.787
7	0.924	0.751

shows the cos θ values for the outermost wire in each superlayer (a group of 6 wires), where θ is the angle between the beam axis and a line to the farthest end of the wire. Figure 24 shows the number of tracks found versus cos θ for data and MC. A drop-off with increasing θ is apparent. One can also see that the MC doesn't estimate the efficiency very well for $|\cos\theta| > 0.82$. Therefore a cut was set at that value.

4.2.2 Neutral Shower Cuts

The barrel and endcap electromagnetic calorimeters were used to detect showers from electrons, positrons and photons. The reconstruction program first extrapolated the found charged tracks into the calorimeters and associated energy deposits with them. The program then examined the unused deposits and formed tracks if they were consistent with a particle coming from the inner part of the detector.

Each reconstructed shower that was not associated with a charged track was examined. To be well contained within the fiducial volume of the calorimeter, the showers found in the barrel must have had $|\cos\theta| > 0.68$ and the centers must have been projected to be at least one strip away from the 3° cracks between the modules.

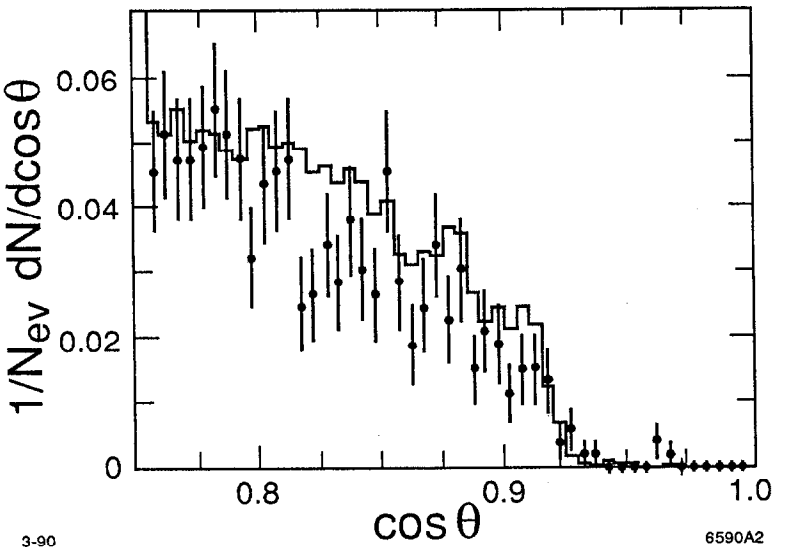

Figure 24: The cos θ values for tracks in the data (points) and the MC simulation (histogram).

For the endcaps, the angular requirement was that $0.74 > |\cos\theta| > 0.95$. A shower energy of at least 0.5 GeV was also required.

4.3 Event Cuts

The tracks and showers selected above were used to make the event cuts. The first requirement was that there be at least 5 quality charged tracks in the event. Most lepton pair events and cosmic, two-photon and beam-gas events (see the next section for explanations of these types of events) are eliminated with this cut. A further cut was necessary to avoid including $\tau^+\tau^-$ pairs which can have a total of 6 charged tracks if both τ particles decay to 3 charged particles (*e.g.* $\tau^- \rightarrow \pi^-\pi^-\pi^+$). For events with 5 or 6 charged tracks, the event was divided into two hemispheres using the thrust direction (see Chapter 5) as an approximation to the τ direction. If the invariant

mass of the charged particles on either side was less than 2.0 GeV, then the event was rejected as a probable τ candidate. There were very few of these type of events produced, so this effect was small.

The visible energy in the event was defined as

$$E_{vis} = \sum_{ch} \sqrt{(p^2 + m_\pi^2)} + \sum_{neu} E_{neu}.$$

The final cut was that E_{vis} must be $\geq 0.4 E_{cm}$. In addition to removing possible two-photon candidate events, the cut also had the advantage of ensuring that most of the particles in the event were measured. Thus the number of distorted events in the sample was minimized.

4.4 Background Estimates

The contamination in the sample from other sources was estimated. Those sources were divided into two types - physics backgrounds and environment backgrounds.

4.4.1 Physics Backgrounds

The first type of background comes from physics processes that occur in e^+e^- annihilation but are not the ones under study. The main processes involved are pictured in Figure 25 and are lepton pair production (τ pair being the most serious) and two-photon events. MC simulations of these processes were used to generate 1.7 and 248 pb^{-1} of events, respectively. A small number of these events passed the cuts listed above, which corresponded to a contamination in the data sample of 0.26 events for τ pairs and 0.16 events for two-photon events.

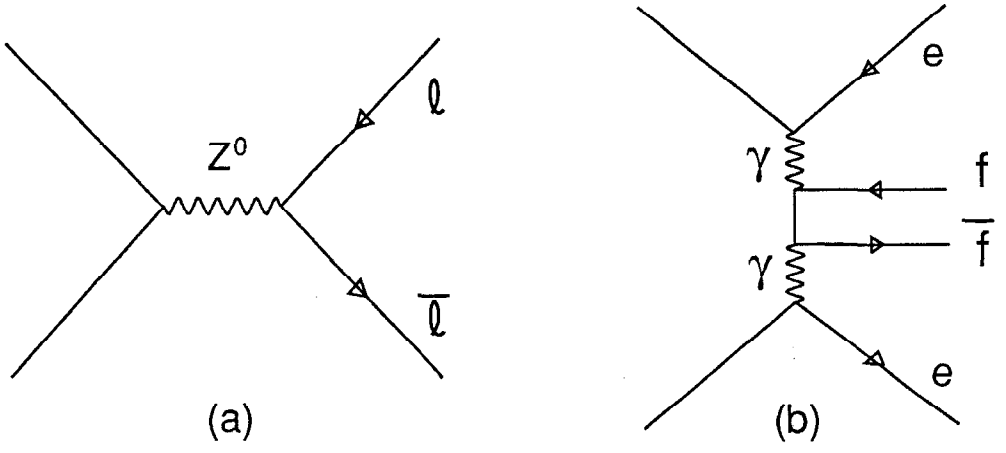

Figure 25: Feynman diagrams for the physics processes considered as background for this analysis: a) lepton pair production and b) two-photon events.

4.4.2 Environment Backgrounds

There can also be backgrounds caused by the environment around the detector. These can either be whole events that mimic a hadronic decay of the Z^0 at the triggering level or information that is superimposed on a true Z^0 decay. Two sources of background events were cosmic ray and beam-gas events. The number of cosmic ray events that passed the cut of five or more tracks was negligible. However, beam-gas events (when an electron or positron in the beam interacts with the gas inside the beam pipe and produces a spray of particles in the detector) were examined more closely.

An estimate of the number of beam-gas events was made by searching through the DST sample with all event cuts except the requirement on the z position of the tracks. (The beam-gas events can occur at any z position in the beampipe.) Charged tracks were accepted if the z coordinate was within 0.50 m of the IP (*cf* 0.03 m for the usual analysis). There were 0 events that passed this relaxed set of cuts which

corresponds to a 95% confidence level upper limit of less than 0.4 beam-gas events in the data sample.

The effects of stray particles hitting the detector which were superimposed on events must also be dealt with. These particles were generated whenever the beam particles hit beamline components before they reached the detector. The stray particles consisted of muons, photons from synchrotron radiation and other forms of electromagnetic debris. The technique used to help adjust for the extra energy and hits in the detector is called "mixing". After MC generated events have undergone the full detector simulation, the information from random beam crossings that were recorded near in time to the Z^0 decays was mixed in at the raw data level. Then the mixed events were passed through the standard track and shower reconstruction algorithms. In this way it is hoped that a compensation was made for the machine environment.

4.5 Summary of Sample

After all track, shower and event cuts there was a total of 398 hadronic Z^0 decays. As detailed above, a total background of 0.8 events was estimated due to τ pair production, beam-gas backgrounds and two-photon production.

4.6 Corrections

The quantities that were measured in the detector have been changed from their true value by many different effects. A correction must be made for these effects before a meaningful measurement of physics processes can be presented. In this case the decay of Z^0 bosons to quarks and their subsequent hadronization was being examined.

The ability to measure this decay was hampered by, for example, the fact that the detector didn't capture each outgoing particle (acceptance), or that there was a finite resolution for a given measurement. These can be summed up as detector effects. As discussed before, there were unwanted particles entering the detector due to the machine environment. It was also necessary to correct for the process of initial state radiation.

To quantitatively estimate these effects, a detailed Monte Carlo simulation of the detector and the environment was written for each system in the detector. For an event produced by the models described in Chapter 2, each particle was tracked through the detector and suitable information was generated which is equivalent to the raw data. This raw information was then analysed by the same programs that were used for the data. The result was the ability to compare, on an event basis, the model-generated information with what was seen in the detector.

The simplest way to correct a detected (or observed) distribution back to a generated distribution is to correct each bin individually. This bin-by-bin correction is a valid procedure only if the quantity being studied is not changed very much by the detector simulation. For each bin, a correction factor $C(x)$ is determined with

$$C(x) \equiv \frac{n_{gen}(x)/N_{gen}}{n_{det}(x)/N_{det}},$$

where $n_{gen}(x)$ is the number of entries in bin x of the generated distribution, $n_{det}(x)$ the entries in the detected distribution and N_{gen} and N_{det} the total number of generated and detected events, respectively. In general, N_{gen} is larger than N_{det} as some events are lost due to detector acceptance. Ideally, the correction factors are close to 1, or at least vary little from bin to bin. To obtain the corrected distribution, one uses the relation

$$n_{cor}(x) = C(x)n_{obs}(x)$$

where $n_{obs}(x)$ is the measured number of events in bin x. For the results in this report, the JETSET shower model was used to calculate the correction factors. The differences when other models were used were incorporated as a systematic error on the correction factor. The other main systematic error was to account for possible errors in the way the effects of the backgrounds in the detector were estimated (see section 4.4.2). The uncertainty in the correction factors was evaluated by calculating the difference in the correction factors with the random beam crossings mixed in and without, then dividing that value by 4.

Chapter 5

Event shapes

The underlying parton structure in an event has consequences for the overall energy and momentum flow of the resulting hadrons. One class of observables that measures these global event characteristics are loosely termed shape variables. In this chapter some common variables are presented along with their distributions at 91 GeV. Also shown are how the mean values change over a range of center-of-mass energies.

5.1 Definition of Observables

Only a few of the many different types of shape variables have been chosen for study. They are: sphericity (S), aplanarity (A) [57], thrust (T) [58], the heavy hemisphere mass (M_h) and the light hemisphere mass (M_l). The first three distributions have already been shown based on a smaller sample of data [59].

Both the sphericity and the aplanarity are derived from the energy-momentum tensor,

$$M_{\alpha\beta} = \frac{\sum_i p_{i\alpha} p_{i\beta}}{\sum_i p_i^2}$$

with α, β denoting the three coordinates of the momentum and i running over all particles. When this tensor is diagonalized, the result is three eigenvectors $(\hat{n}_1, \hat{n}_2, \hat{n}_3)$ and three eigenvalues (Q_1, Q_2, Q_3), with $Q_1 < Q_2 < Q_3$. The eigenvectors $\hat{n}_3$ and $\hat{n}_2$ define the "event plane" which typically contains most of the momentum of the event. The sphericity is defined as $S = \frac{3}{2}(Q_2 + Q_1)$ and has the range 0 to 1. An event that has no preferred direction (*ie* spherical) will have S=1 whereas a tightly collimated 2-jet event will have S approaching 0. The aplanarity is defined as $A = \frac{3}{2}Q_1$ and measures the amount of momentum out of the event plane. A Z^0 decay which produces 3 partons (*e.g.* $q\bar{q}g$) will be essentially planar due to momentum conservation. Therefore the aplanarity measures the number of 4–parton events and also the amount of momentum given to the hadrons during the fragmentation process. The advantage of these two shape variables is that they are quite easy to calculate. The disadvantage of them rises from the quadratic momentum dependence; high momentum particles are weighted heavily. Also they are not what is termed "collinear safe". If one particle decays into two almost collinear particles, then the sphericity would change, although the underlying energy flow is the same.

The thrust is a quantity that is linear in momentum and does have the property of being collinear safe. Again, a coordinate system is chosen in the event. In this case, an axis $\hat{n}_1$ is found that maximizes the quantity

$$T = \frac{\sum_i |p_{i\|}|}{\sum_i |p_i|}$$

where i runs aver all the particles and $p_{i\|}$ is the component of momentum along $\hat{n}_1$. T is then called the thrust. The second axis maximizes momentum in a direction perpendicular to $\hat{n}_1$ and the third defines an orthogonal system. For the predominant 2-jet events the thrust peaks near 1, so we have chosen to show the quantity 1-T. The two coordinate systems defined in these ways (sphericity axes and thrust axes)

are used later in the charged-particle inclusive studies.

Two other interesting quantities that give information about the shape of the event are the invariant masses in each "side" of the event. To calculate these, the event is divided into two hemispheres along the thrust axis. The sum of the 4-momenta of all the particles in a given hemisphere is formed and the associated invariant masses $m_{inv}^2 = E^2 - p^2$ is calculated. The results from the two sides are compared and the largest is defined as M_h^2, the heavy mass, and the other as M_l^2, the light mass. These variables also have the property of being collinear safe. In this report the scaled heavy mass M_h^2/s and the scaled difference in the masses $(M_h^2/s - M_l^2/s)$ are studied. As the full center-of-mass energy wasn't detected, the masses were normalized to the visible energy. These quantities are of interest as, along with thrust, they can be calculated at the parton level using perturbation theory. The difference between using partons and hadrons is small as the 4–vectors of the decay products are summed to form the invariant masses.

5.2 Observations

Using the event sample described in the previous chapter, the distributions for S, 1-T, A, M_h^2/s and $(M_h^2/s - M_l^2/s)$ were calculated. These raw distributions were affected by detector resolution and acceptance and by the event cuts made. The procedure described in section 4.6 was used to make corrections for each bin.[1] Tables 8 and 9 show the bin ranges and correction factors for each of the shape distributions.

[1]Some experiments that have calculated these quantities [60] have used a more complicated correction procedure than the bin-by-bin correction for the scaled invariant masses. As mentioned in section 4.6, the procedure is only valid if there is little shifting among the bins. This data sample is small enough that the bins must be large and the simpler correction procedure is valid.

Table 8: Correction factors for each bin for the shape distributions S, A, (1-T).

	Sphericity		Aplanarity		1-Thrust	
Bin	range	factor	range	factor	range	factor
1	0.00-0.02	1.22	0.000-0.004	1.23	0.00-0.01	0.57
2	0.02-0.04	0.99	0.004-0.008	1.18	0.01-0.02	1.15
3	0.04-0.06	0.93	0.008-0.012	0.94	0.02-0.03	1.26
4	0.06-0.10	0.85	0.012-0.016	0.85	0.03-0.04	1.12
5	0.10-0.20	0.89	0.016-0.024	0.80	0.04-0.05	0.99
6	0.20-0.30	0.93	0.024-0.060	0.70	0.05-0.06	0.90
7	0.30-0.40	0.91	0.060-0.140	0.62	0.06-0.08	0.91
8	0.40-0.60	0.77	—	—	0.08-0.10	0.92
9	—	—	—	—	0.10-0.15	0.92
10	—	—	—	—	0.15-0.20	0.94
11	—	—	—	—	0.20-0.30	0.84

Table 9: Correction factors for each bin for the shape distributions M_h^2/s and $(M_h^2/s - M_l^2/s)$.

	Heavy mass		Mass difference	
Bin	range	factor	range	factor
1	0.000-0.016	0.78	0.000-0.008	1.17
2	0.016-0.024	1.27	0.008-0.016	1.12
3	0.024-0.032	1.12	0.016-0.024	0.94
4	0.032-0.040	1.00	0 024-0.032	0.92
5	0.040-0.056	0.99	0.032-0.040	0.91
6	0.056-0.072	0.94	0.040-0.056	0.86
7	0.072-0.104	1.01	0.056-0.072	0.95
8	0.104-0.136	1.00	0.072-0.104	0.90
9	0.136-0.216	0.97	0.104-0.136	0.84
10	—	—	0.136-0.216	0.95

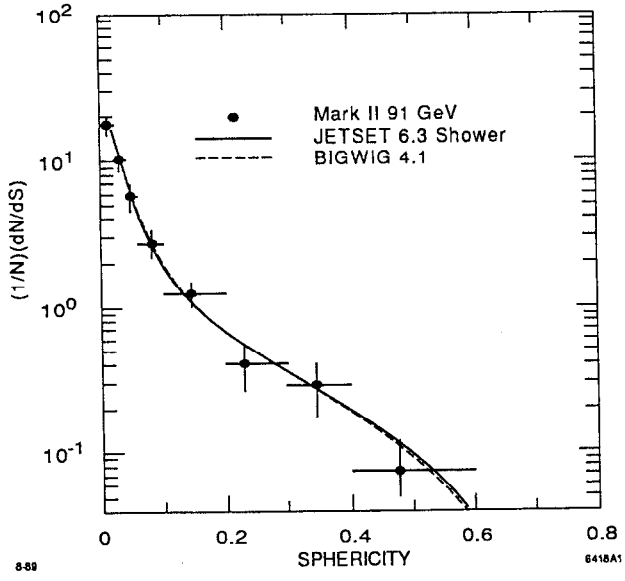

Figure 26: Corrected sphericity distribution 1/N dN/dS.

The corrected distributions are shown in Figures 26 to 30 along with the predictions from the QCD Monte Carlo models discussed in Chapter 2. In general, the models with their parameters tuned at E_{cm}= 29 GeV do a very good job describing the shape distributions. With the statistical precision of this data sample, neither of the models show a significant deviation from data.

The sphericity distribution in Figure 26 shows that the events in general have a low sphericity, that is, they are 2-jet-like. This is also apparent in the 1-T distribution, Figure 27, as it is peaked very close to 0 which means that most of the momentum is along one axis. The aplanarity in general is low as well, but is not 0. This implies that although most of the events are planar, there is a measurable number of events that have momentum flow out of the event plane. The invariant mass distributions are shown in Figures 29 and 30.

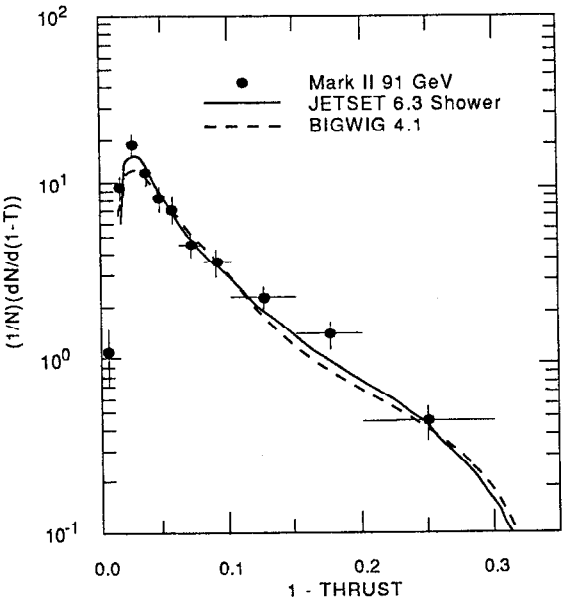

Figure 27: Corrected 1-Thrust distribution 1/N dN/d(1-T).

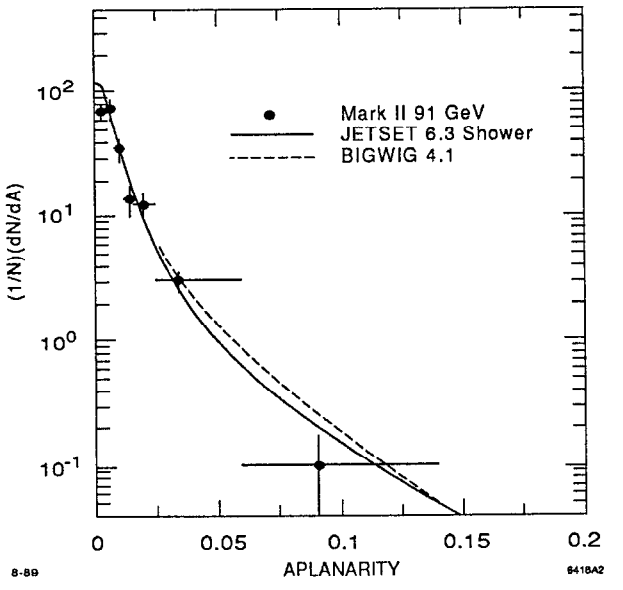

Figure 28: Corrected aplanarity distribution 1/N dN/dA.

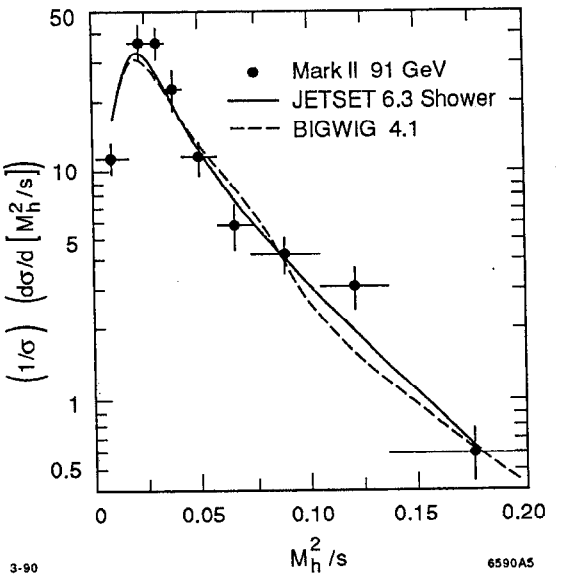

Figure 29: Corrected scaled invariant heavy mass distribution.

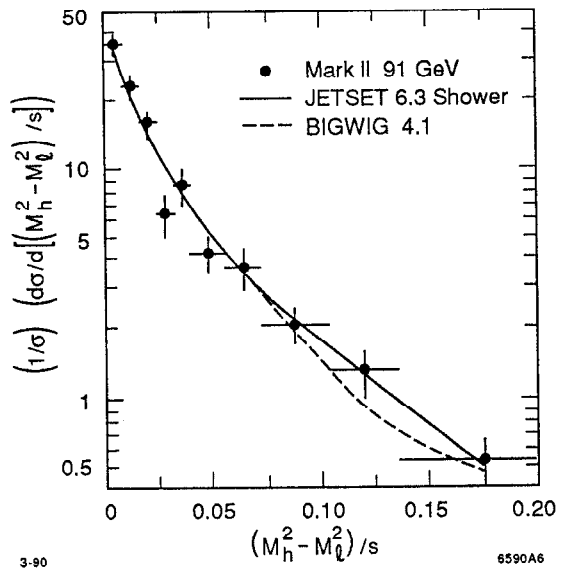

Figure 30: Corrected distribution of the difference between the scaled invariant heavy and light masses.

5.3 Variation with E_{cm}

The shape distributions change significantly when the center-of-mass energy changes. In Figure 31 is shown the mean values of S, 1-T, and A as a function of the center-of-mass energy as measured by several e^+e^- experiments [60,61,62,63,64]. The values measured by Mark II at 91 GeV are $< \mathrm{S} >= 0.075 \pm 0.005$, $< \mathrm{A} >= 0.0113 \pm 0.0007$, and $< 1 - \mathrm{T} >= 0.068 \pm 0.003$. As E_{cm} increases, the partons have more energy and the resulting hadrons are more energetic and collimated. Thus the sphericity decreases and the mean thrust approaches 1. In addition, the coupling constant decreases and one would expect fewer four-jet events. Therefore the aplanarity is also expected to decrease. These expectations are realized by the measurements. The measured variation of the scaled invariant masses is shown in Figure 32 compared with other experiments [60,62] and the JETSET shower model. The values from the data in this report are $< M_h^2/s >= 0.053 \pm 0.002$ and $< (M_h^2/s - M_l^2/s) >= 0.035 \pm 0.002$. The heavy scaled invariant mass is expected to vary in a similar manner to the thrust as E_{cm} increases. The difference in the scaled invariant masses should be sensitive to gluon radiation (high values of M_h^2/s are caused by 3–jet events) therefore a slight decrease of the mean value is expected as E_{cm} changes. These predicted variations are also seen. More study would be needed to determine the relative contributions of the increasing parton energy, the decrease of α_s and the energy-independent fragmentation effects to the variation of the shape variables shown.

The above energy variation arguments only apply as long as a threshold to produce new particles is not crossed. Some of the first techniques explored to search for new particle production in Z^0 decays used shape variables. For example, a heavy top quark t would yield very spherical events from $Z^0 \rightarrow t\bar{t}$. Therefore one would expect the mean sphericity to be significantly higher than the QCD models with just *udscb*

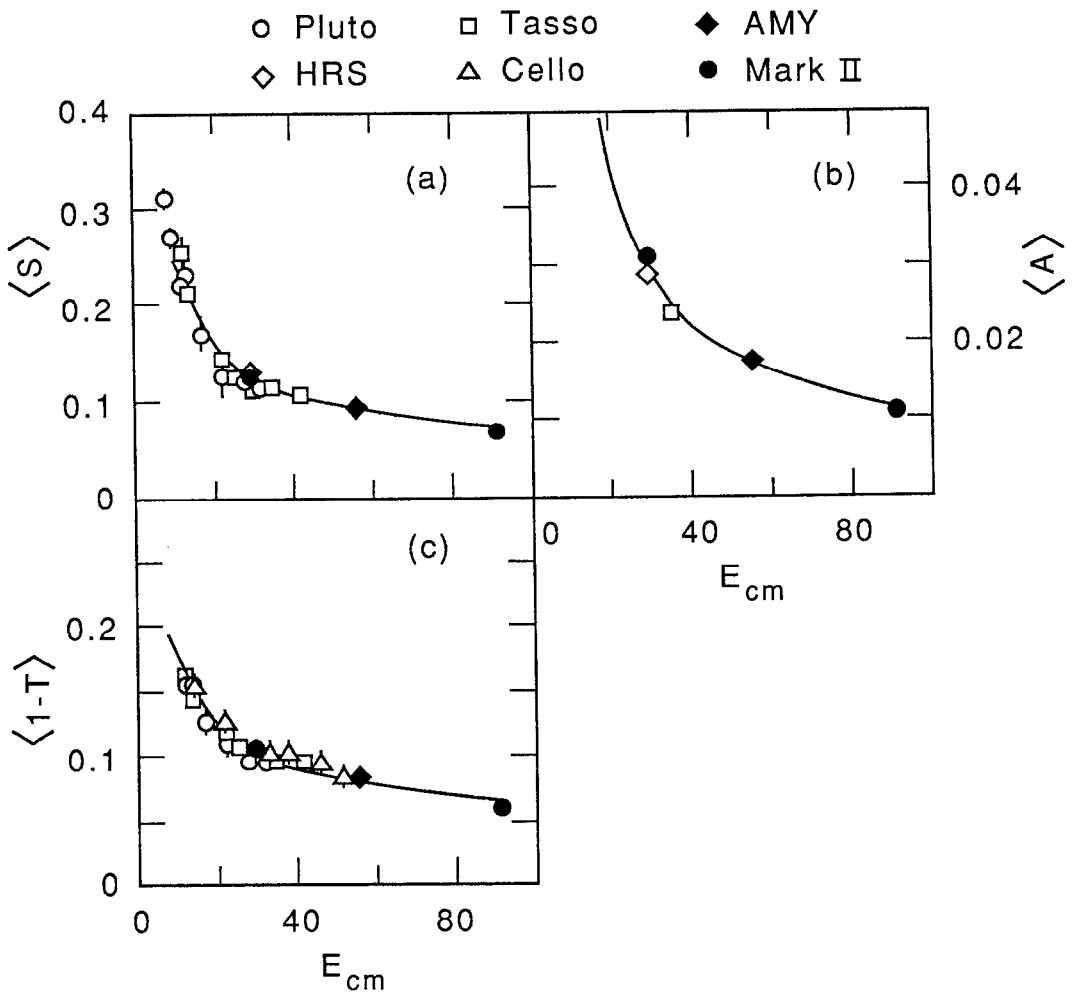

Figure 31: Mean values of sphericity (S), thrust (1-T), and aplanarity (A) versus E_{cm}. The 91 GeV data values are compared with those from lower energy e^+e^- experiments; the solid lines are from the JETSET 6.3 shower model.

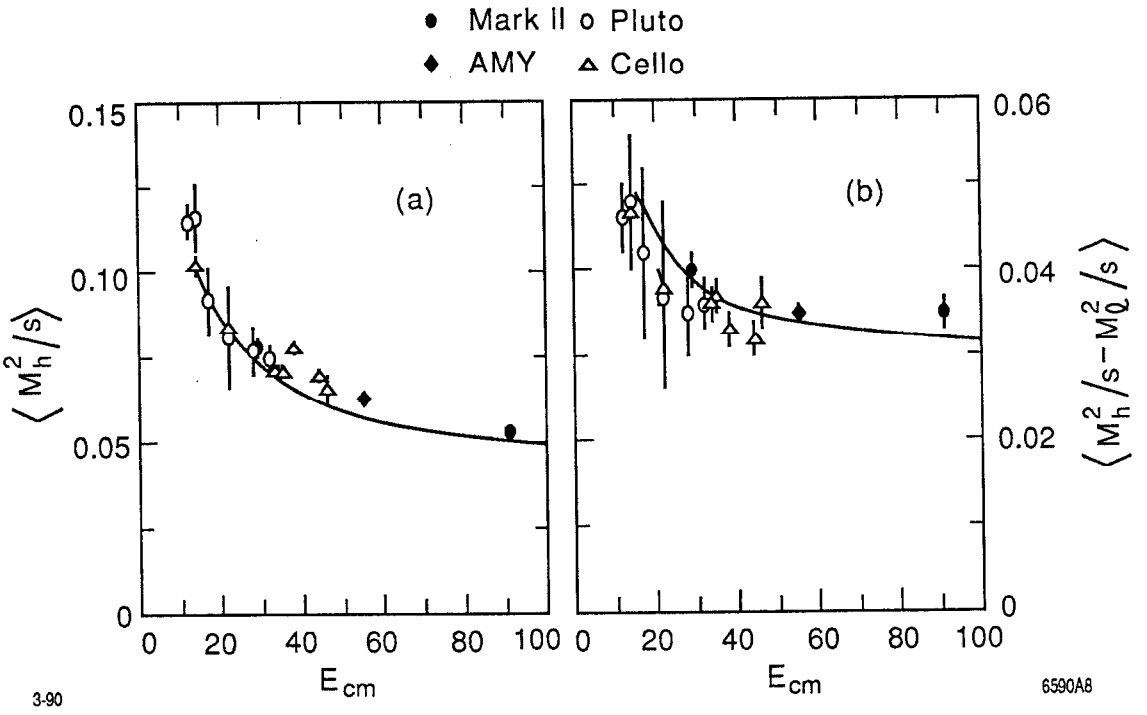

Figure 32: Mean values of M_h^2/s and $(M_h^2/s - M_l^2/s)$ vs E_{cm}. The solid line is the JETSET 6.3 shower model.

quarks would predict. However, due to the variation of predictions from the different models, other techniques were developed. So far there is no evidence for new particle production [65].

Chapter 6

Jet Multiplicity

The concept of a "jet" is an intuitive tool that helps equate the particles seen in the detector with the initial quarks and gluons produced in the decay of a Z^0. In Figure 33 a reconstruction of an event in the detector is shown. Three sprays of particles can be clearly seen; they are called jets and associated with partons being produced. In practise, however, it is not always easy to reconstruct the partons from the hadrons. The first section in this chapter discusses the algorithms which find the jets. The second and third sections then discuss the jet-like properties of hadronic Z^0 decays and how they vary with center-of-mass energy.

6.1 Cluster Algorithms

The shape algorithms described in Chapter 5 were the first attempts at looking at the underlying parton structure of events. The existence of 3-jet events at PETRA [66] was shown by various algorithms. However, many of these algorithms assumed that one was looking for 3-jet events and used the properties of this class of events (*e.g.* planarity) to construct the jets. For a general analysis tool, it is useful to have

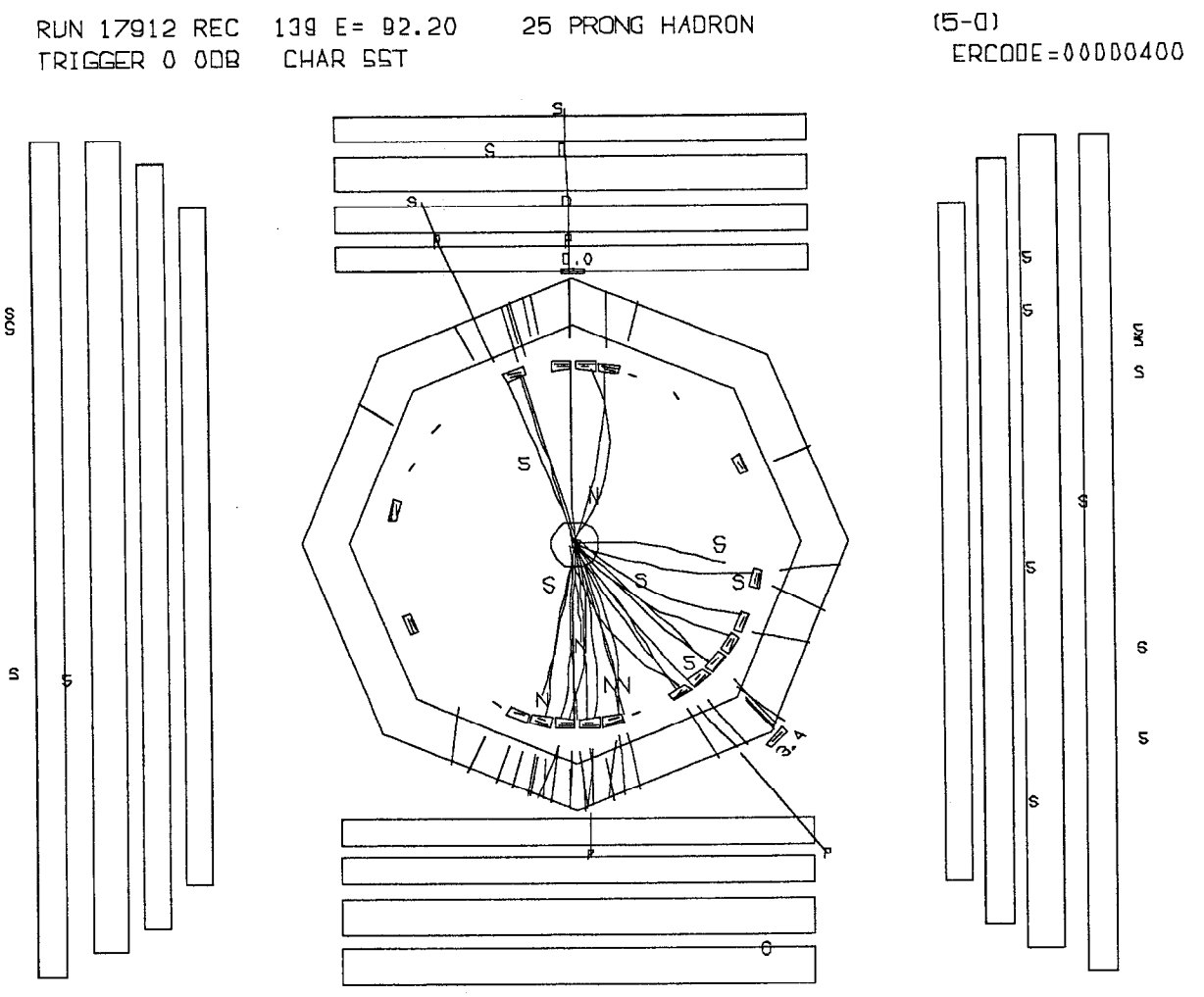

Figure 33: End-on view of an event in the Mark II detector showing a 3–jet event.

a jet-finding algorithm that has some criterion that will yield a varying number of jets.

The algorithms discussed below are often called cluster algorithms because they cluster the particles in an event together until the clusters reach a certain size or separation from each other. Therefore the number of jets the algorithm will find depends on some separation parameter, usually called the jet resolution parameter. It is quite common to show the variation in the number of jets as the parameter varies.

As the name suggests, the jet resolution parameter is supposed to deal with cases where the jets are close together and it may not be possible to tell if there are two small jets or one large one. This would seem to imply that there is a fixed absolute cutoff that would be determined by experimental factors. However, the energy of the partons themselves is (approximately) scaling with E_{cm}. Therefore, if an algorithm that can match the hadron jets with the underlying partons is desired, it is reasonable to scale the jet resolution parameter with E_{cm} as well.

Two algorithms that are widely used are the clustering algorithm supplied with JETSET (LCLUS) [67] and a clustering algorithm developed by the JADE experiment (YCLUS) [68]. Both algorithms give a varying number of clusters as the default.

6.1.1 Algorithm Descriptions

LCLUS

The LCLUS clustering algorithm uses the momenta of the particles. Ideally, the cluster algorithm goes as follows. Initially each particle is treated as its own cluster. A distance D is calculated between cluster i (momentum $\vec{p}_i$) and cluster j (momentum

$\vec{p}_j$) with

$$D = \sqrt{\frac{2|p_1|^2|p_2|^2(1-\cos\theta_{12})}{(|p_1|+|p_2|)^2}}$$

where θ_{ij} is the angle between jets i and j. For small angles θ_{ij}, this reduces to

$$D \approx |\vec{p}_i \times \vec{p}_j|/|\vec{p}_i + \vec{p}_j|$$

which is the transverse momentum of either particle with respect to the vector sum of the two momenta. The two clusters that have the smallest value of D are joined together and the procedure is repeated until the values of D for all clusters is above d_{join}, the jet resolution parameter. The default value of d_{join} tuned at $E_{cm} = 30$ GeV is 2.5 GeV, giving a scaled value of 7.9 GeV at $E_{cm} = 91.1$ GeV.

In practise, the algorithm is sped up by setting up an initial configuration of up to 8 clusters. Also, after each joining of clusters, the particles can be reassigned if they have become closer to one of the new cluster directions.

YCLUS

The YCLUS algorithm uses the invariant masses of the particles and jets to determine if they should be joined together. It is based on the method used when avoiding infrared divergences while calculating matrix elements (see section 2.3.2), substituting the visible energy for the center-of-mass energy. At the start of the algorithm, all particles are treated as clusters. The quantity

$$y = \frac{m_{ij}^2}{E_{vis}^2}$$

is calculated for each pair of clusters. There are two options for the invariant mass calculation,

$$m_{ij}^2 = E_{ij}^2 - p_{ij}^2$$

or

$$m_{ij}^2 = 2E_iE_j(1-\cos\theta_{ij}).$$

The two clusters with the smallest y value are joined together, and this process continues until all of the y values are larger than some y_{cut}, the jet resolution parameter. Typical values for y_{cut} are between 0.02 and 0.10. In addition to the similarity to the calculation, it is also a conceptually simple algorithm and is easy to implement.

6.1.2 Algorithm Comparison

The two algorithms were compared using two sets of MC events. The first set was generated with JETSET 6.3 using matrix elements to generate the partons and then string fragmentation to generate the hadrons. As only 2–4 partons are produced, this allows a direct comparison between the partons and the jets found when the algorithm is applied to the hadrons.

The second set of events was generated with JETSET 6.3, using the shower algorithm for the partons. This process generates, on average, 11 partons at E_{cm}= 91 GeV. Thus the clustering algorithm must be used on the partons themselves before they can be compared to the jets from the hadrons. The YCLUS algorithm copies the procedure used when combining partons analytically, therefore that algorithm was used with a typical y_{cut} value of 0.015 to calculate the shower "partons" for the matching.

For this analysis, it was desired that the jets found reflect the underlying parton structure. Therefore the number of jets should match the number of partons; also the found jets should match the partons in direction and energy. For studying changes in jet structure with E_{cm}, it is also useful to have the correspondence between partons and jets be constant with respect to changes in E_{cm}.

The first measure of the algorithms was to determine the percentage of events where the algorithm found the same number of hadron jets as there were partons. For

Table 10: Results of the jet algorithm comparison at $E_{cm} = 91$ GeV.

partons		JETSET matrix elements			JETSET shower (clustered)		
algorithm		YCLUS opt 1	YCLUS opt 2	LCLUS	YCLUS opt 1	YCLUS opt 2	LCLUS
% match		69.5	50.2	42.5	69.3	59.5	52.1
mean	1	0.90	0.95	0.88	1.19	1.12	1.00
angle	2	1.70	1.31	1.26	2.21	1.62	1.46
diff	3	16.80	8.30	3.90	19.51	11.15	5.90
(deg)	4	23.49	9.83	6.17	27.24	12.64	9.43
mean	1	0.05	0.04	0.03	0.05	0.04	0.03
energy	2	0.08	0.05	0.04	0.08	0.05	0.04
diff	3	0.32	0.17	0.07	0.27	0.17	0.10
Δ_E	4	0.34	0.17	0.08	0.31	0.21	0.15

those that matched, it was then possible to determine the quality of reconstruction. The partons (or clustered partons for the shower MC case) were matched with the hadron jets by pairing the highest energy parton with the closest hadron jet. This procedure continued for each of the remaining partons and jets. The angle between the first pair by construction was be small. However, the comparison of the angle between the other pairs is a test of the algorithms. The energies were also compared, with the parton energy E_p scaled to E_{cm} and the jet energy E_j scaled to E_{vis}. The quantity

$$\Delta_E = \frac{2(\frac{E_p}{E_{cm}} - \frac{E_j}{E_{vis}})}{(\frac{E_p}{E_{cm}} + \frac{E_j}{E_{vis}})}$$

was calculated for each match.

The results at 91 GeV are summarized in Table 10 for the two algorithms (with two options for the invariant mass in YCLUS) and the two versions of parton generation. The jet resolution parameter for LCLUS had a value of 7.9 GeV and YCLUS, $y_{cut} = 0.04$ was used (other values gave similar conclusions). In general, the version of YCLUS that uses the first option to calculate the invariant mass had more events in

Table 11: Comparison of the two algorithms as E_{cm} is changed.

	YCLUS option 2		LCLUS		
E_{cm}	% match	$f_3(parton)/f_3(hadron)$	% match	$f_3(parton)/f_3(hadron)$	d_{join}
29	45.1	0.96	38.8	1.24	2.5
40	52.9	1.03	46.9	1.34	3.5
50	53.9	1.09	48.7	1.37	4.3
60	54.2	1.17	32.4	1.47	5.2
70	56.7	1.18	50.5	1.52	6.0
80	56.7	1.34	50.9	1.80	6.9
91	59.5	1.37	52.1	1.85	7.9
100	62.4	1.40	54.5	1.84	8.6

which the number of jets and partons match. However, the angle and energy of the reconstructed hadron jets differed considerably from the partons. This option will not be considered further.

The other two algorithms tested, YCLUS with the second option and LCLUS, gave very similar results. They differed in that the first gave more events where the number of jets and partons matched and the second had a slightly better quality of reconstruction. The next quality factor, namely the quality of the parton-hadron match as the energy changes, was examined. For this study, the JETSET shower MC was run for a range of energies, then the partons were clustered with $y_{cut} = 0.015$ (other values gave the same results). At each energy, the events with the number of hadron jets equal to the number of clustered partons were counted. Also, the ratio of 3–parton events to 3–hadron jet events was calculated. The results are in Table 11, and show that the YCLUS algorithm produces a higher percentage of events with equal numbers of jets as well as a smaller variation in the ratio. Therefore, as the quality of the match is not too dissimilar, this form of the algorithm was chosen for the jet analysis.

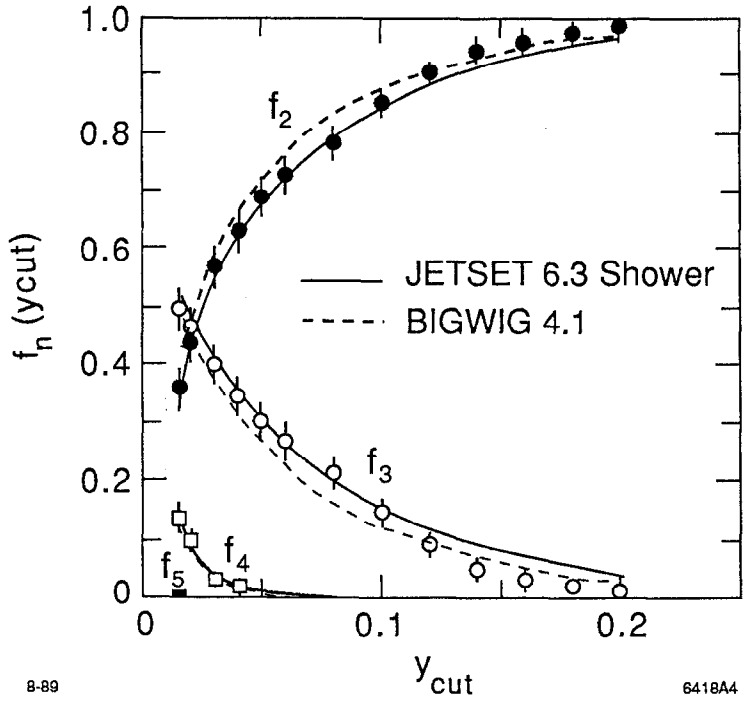

Figure 34: Jet fractions as a function of y_{cut}. The solid line is from the JETSET 6.3 model, the dashed line from BIGWIG 4.1.

6.2 Jet Fractions

The goal is to measure the number of n–jet events and compare the results with the model predictions. Define

$$f_n = \frac{number\ of\ n-jet\ events}{total\ number\ of\ events},\ n = 1,5$$

as the jet fractions. For each value of y_{cut}, the uncorrected values of f_1 to f_5 were determined. Corrections for detector acceptance, initial state radiation and event cuts were extracted from the MC simulation. The corrected values are in Figure 34. The solid line is the JETSET shower model and the dashed line is the BIGWIG 4.1 model. Each set of points at a given y_{cut} value uses all of the events, so the different

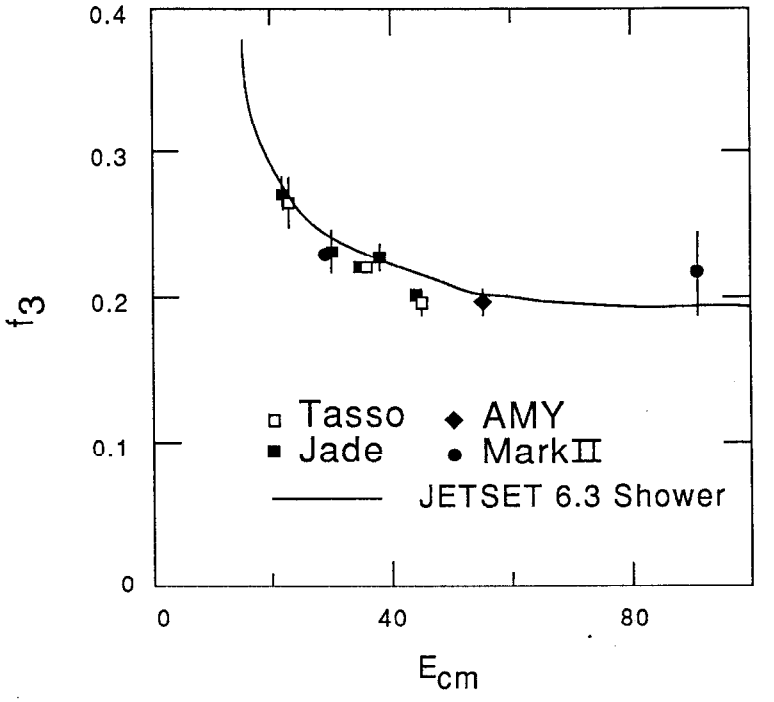

Figure 35: The 3–jet fraction vs E_{cm}.

y_{cut} points are not statistically independent. For a given value of y_{cut}, it can be seen that both models are within 2σ of the data, with the JETSET shower model being closer. At a typical y_{cut} value of 0.04, we have 60% 2–jet events, 37% 3–jet events and 3% 4–jet events.

It is also interesting to see the variation with E_{cm} of the jet fractions. The variable f_3 is chosen because, in first order, the number of 3–jet events is proportional to α_s. The coupling constant is expected to decrease with an increase in E_{cm}, so f_3 is expected to decrease as well. Figure 35 shows f_3 vs E_{cm} for several experiments with the jet resolution parameter at $y_{cut} = 0.08$ [69], along with the results with the JETSET shower prediction. With the large error it is difficult to confirm that the values are still decreasing, but the data is consistent with that expectation.

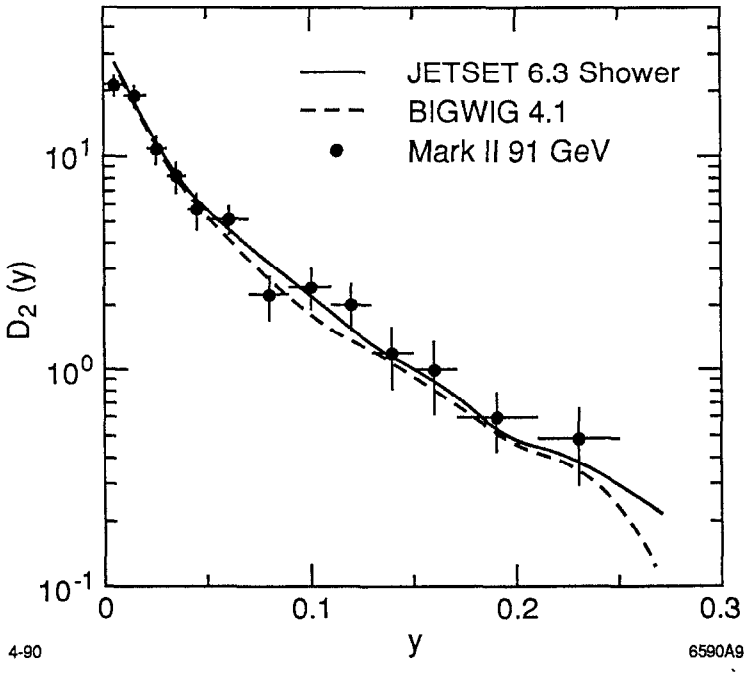

Figure 36: Corrected differential jet distribution $D_2(y)$.

6.3 Differential Distribution

Another way of displaying the information about 3–jet events is to take the derivative of the f_3 distribution in Figure 34. Rather than measuring the fraction at a fixed y_{cut}, the value of y at which the event transforms from a 3–jet event to a 2–jet event is found. Or equivalently, the minimum invariant mass of the 3 possible combinations of the 3 jets is found. The advantage to this method of looking at jets is that each event enters only once into the distribution and therefore analyses of the match between data and the models is more straightforward.

The function $D_2(y)$ is defined to be the distribution of y values for which the events go from 3– to 2–jet. The data values are shown in Figure 36 along with the models. Again, the models predict the behaviour of the data.

Chapter 7

Inclusive Charged Track Distributions

This chapter concentrates on the information given by the charged tracks in the event. Examining the multiplicity, the momenta and the flow of the momenta in the event gives clues about the mechanism that takes the partons to the detected hadrons. The data in the first three sections has been previously published [70].

7.1 Charged Multiplicity

One of the obvious measurements to make about a group of events is to measure the average number of charged particles produced. A mean charged-particle multiplicity that has been corrected for detector effects was measured from the hadronic event sample.

7.1.1 Corrections

Most of the charged particles produced in an event at this E_{cm} have momenta below 1 GeV/c (see section 7.2). Unfortunately, these particles are also the most susceptible to being scattered by the material in the detector, which means the tracks are more difficult to reconstruct. In addition, tracks of all momenta are simply not seen if the particle exits the ends of the detector. Due to these and other reasons, it was not possible to use the bin-by-bin corrections described in section 4.6 as the correlation between bins is large. For example, over 50% of Z^0 decays with 20 charged particles produced will only have 11–16 charged particles measured.

The correction method used to obtain the mean charged-particle multiplicity was an unfolding technique [61]. A distribution of observed multiplicities was measured which must be corrected back to the original produced charged-particle multiplicity distribution. One choice that must be made is how to correct for secondary decays of the produced hadrons. For example, a B meson can decay within a few hundred microns of the IP to several charged particles; the choice is whether to count the B or the decay products. A standard technique is to let particles with lifetimes less than $3 \times 10^{-10} s$ decay; others are assumed stable. The charged particles from all K^0_S and Λ decays were included.

The effects of the detector are modelled by a Monte Carlo simulation; this program was used to produce a transition matrix A to give the probabilities for detecting n_{det} charged particles if n_{gen} are generated. Due to the low statistics of the data sample, several multiplicities were grouped into one entry in the column vector D (for detected) and another grouping was used for G (the generated multiplicity). Therefore in general, A is not a square matrix.

Following a least squares technique [71], a χ^2 variable was defined:

$$\chi^2 \equiv \sum_{i=1}^{n} \frac{1}{\sigma_i^2} (\sum_{j=1}^{m} A_{ij} G_j - D_i)^2$$

where i runs over the detected bins, j runs over the generated bins and σ_i is the error on the detected bin. The solution involved finding the column vector G that minimized the χ^2. Using matrix motation, a diagonal weight matrix W was defined, with $W_{ii} = 1/\sigma_i^2$. Then

$$\chi^2 = (AG - D)^T W (AG - D).$$

The solution was

$$G = V A^T W D$$

with the covariance matrix V defined as:

$$V \equiv (A^T W A)^{-1}.$$

The uncorrected data distribution (grouped) and the result of the unfold are in Figure 37. As the shape information in the corrected distribution is minimal, the detected distribution is compared with the various MC models *after* detector simulation. One can see that the models systematically overestimate the detected multiplicity.

To calculate the mean of the corrected distribution, it is necessary know the value at the center of each bin, b_i. The MC model was used to estimate that number. Then if g_i is the corrected number of entries in each bin,

$$< n_{ch} >= \frac{\sum_i b_i g_i}{\sum_i g_i}.$$

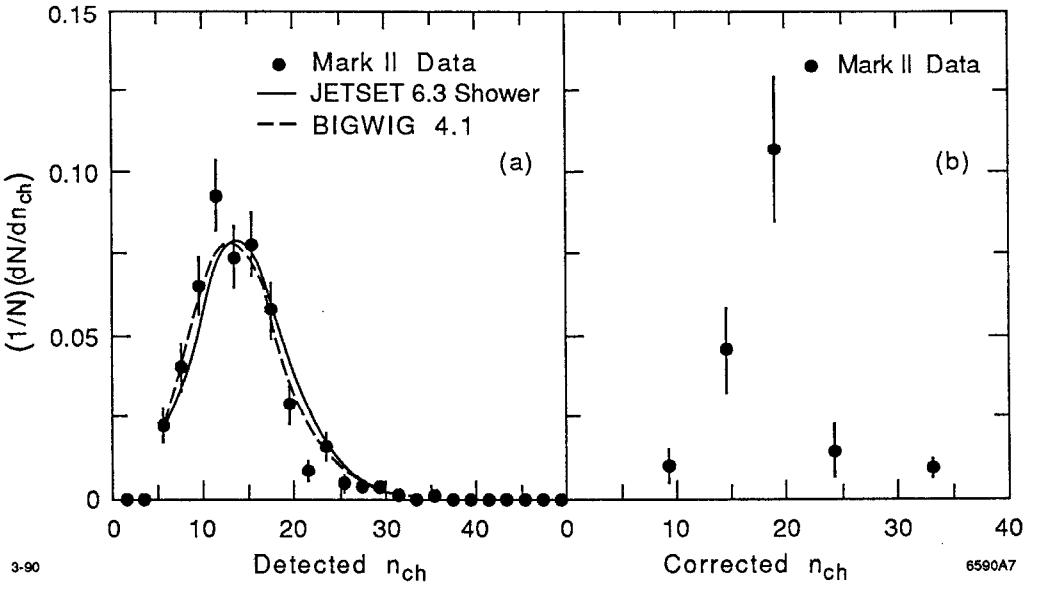

Figure 37: Multiplicity distributions. The uncorrected data is shown in (a), along with the models after detector simulation. The result of the unfold is shown in (b).

7.1.2 Error calculation

The unfold procedure has both a statistical error and a systematic error associated with it. The statistical error was calculated from

$$\sigma^2 = G^T V G$$

and had a value of 1.0. The systematic error from the unfold was generated by grouping the multiplicities in different ways and by using different models to generate the transition matrix A. The resulting spread in the corrected mean gave a systematic error estimate of 0.4. In addition, there was an additional error of 0.8 multiplicity units from uncertainties in the drift chamber efficiency simulation. The final result for the mean corrected charge multiplicity was

$$< n_{ch} >= 19.0 \pm 1.0(stat) \pm 0.9(sys).$$

As a check of this method, a corrected mean was calculated by making a simple overall correction. The mean of the detected data distribution was $13.81 \pm 0.25(stat)$. From the MC simulation, the generated mean is 21.25 ± 0.07 and the detected mean is 14.65 ± 0.06. Using the formula

$$< n_{ch} >_{cor} = < n_{ch} >_{det} \left(\frac{< n_{ch} >_{gen}}{< n_{ch} >_{det}} \right)_{MC},$$

the corrected mean charged multiplicity was calculated to be

$$< n_{ch} >_{cor} = 20.03 \pm 0.36(stat)$$

which confirms the above number. The statistical error from the unfold procedure is higher because the information is spread over more bins.

7.1.3 Variation with E_{cm}

Figure 38 shows the variation of mean charged multiplicity versus center-of-mass energy from e^+e^- experiments [24,61,72,73]. The solid line in the figure is from the JETSET 6.3 shower model. Note that some experiments did not publish a systematic error for their measurement. In those cases only the statistical error is plotted (most errors are smaller than the symbol). The mean charged-particle multiplicity is growing rapidly with E_{cm} and the value at 91 GeV is consistent with the model [1].

7.2 Scaled Momentum

Another interesting property to measure is the momentum of the charged particles. The maximum value possible for a particle to have is E_{beam}. Each hadron would

[1] Several different parameterizations of the energy variation have been proposed in the literature (see *e.g.* [73]) but no fits were made as the large error precludes a precise determination of the fit parameters.

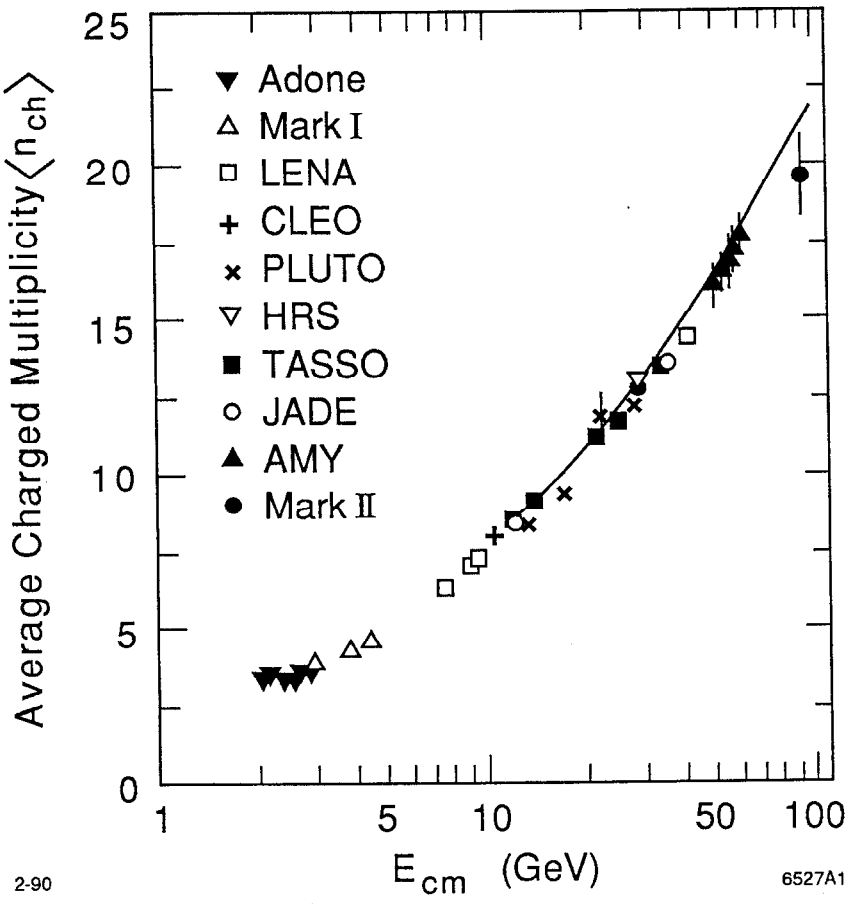

Figure 38: The corrected mean charged-particle multiplicity versus E_{cm} as measured by e^+e^- experiments. The solid line is the JETSET 6.3 shower model.

have that value if only two partons were produced and then they decayed to only one hadron each. The scaled momentum x is defined for charged particles as $x = 2|p|/E_{cm}$. In theory, x has a range of 0 to 1. In practise, the data sample had very few particles with large x.

Without the presence of gluon radiation, the principle of scaling predicts that the distribution $1/\sigma\ d\sigma/dx$ should be the same for all values of E_{cm}. With gluon radiation, the amount of momentum available to the particles from each parton decreases. As the center-of-mass energy increases, a higher number of partons are created and the energy is shared between more particles. Thus the production of high x particles will decrease.

7.2.1 Results

The raw distribution was corrected using the bin-by-bin technique. The correction factors (in Table 12) are very uniform for all but the first bin, which represent particles with momenta below 1 GeV. As mentioned in the previous section, these tracks are subject to large errors in reconstruction. The corrected distribution $1/\sigma\ d\sigma/dx$ is in Figure 39, compared with the results of the two QCD models. The normalization is such that the integral of the curve yields the mean charged multiplicity. The models agree well with the data.

7.2.2 Variation with E_{cm}

To search for evidence of scaling violation, the distribution was divided into bins in x and compared with similar values from other e^+e^- annihilation experiments [24,61,62]. The result is in Figure 40. The solid line in the figure represents the JETSET shower model. The smallest x bin shows a strong rise with E_{cm} due to

Table 12: Correction factors for the charged particle inclusive distributions.

	x		$p_{\perp in}$		$p_{\perp out}$		y	
Bin	range	factor	range	factor	range	factor	range	factor
1	0.00-0.04	1.56	0.00-0.20	1.73	0.00-0.20	1.60	0.0-0.5	2.47
2	0.04-0.08	1.25	0.20-0.40	1.37	0.20-0.40	1.33	0.5-1.0	1.88
3	0.08-0.12	1.25	0.40-0.60	1.26	0.40-0.60	1.24	1.0-1.5	1.49
4	0.12-0.16	1.24	0.60-0.80	1.25	0.60-0.80	1.24	1.5-2.0	1.25
5	0.16-0.20	1.22	0.80-1.00	1.26	0.80-1.00	1.25	2.0-2.5	1.20
6	0.20-0.30	1.32	1.00-1.50	1.26	1.00-1.50	1.33	2.5-3.0	1.20
7	0.30-0.40	1.35	1.50-2.00	1.25	1.50-2.00	1.41	3.0-3.5	1.19
8	0.40-0.50	1.22	2.00-2.50	1.31	2.00-2.50	1.38	3.5-4.0	1.20
9	0.50-0.60	1.20	2.50-3.00	1.30	2.50-3.00	1.21	4.0-4.5	1.09
10	0.60-0.80	1.01	3.00-4.00	1.35	—	—	4.5-5.0	0.79
11	—	—	4.00-5.00	1.53	—	—	—	—
12	—	—	5.00-7.00	1.61	—	—	—	—
13	—	—	7.00-9.00	1.44	—	—	—	—

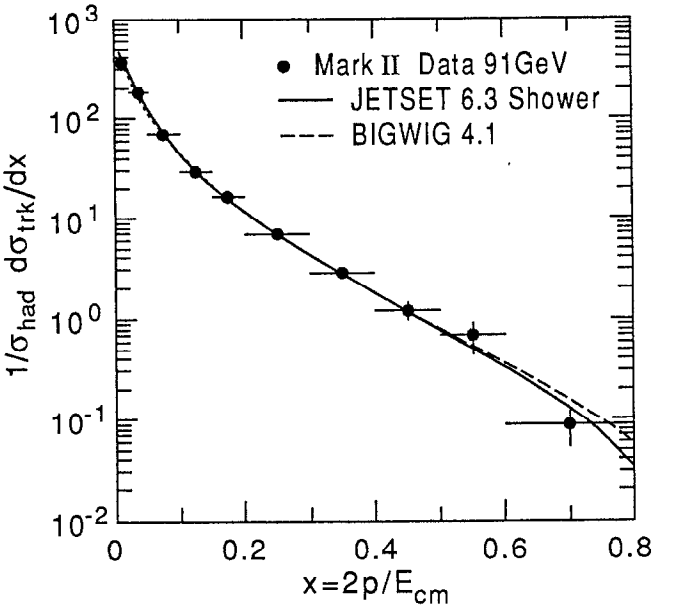

Figure 39: Corrected $1/\sigma\ d\sigma/dx$ distribution.

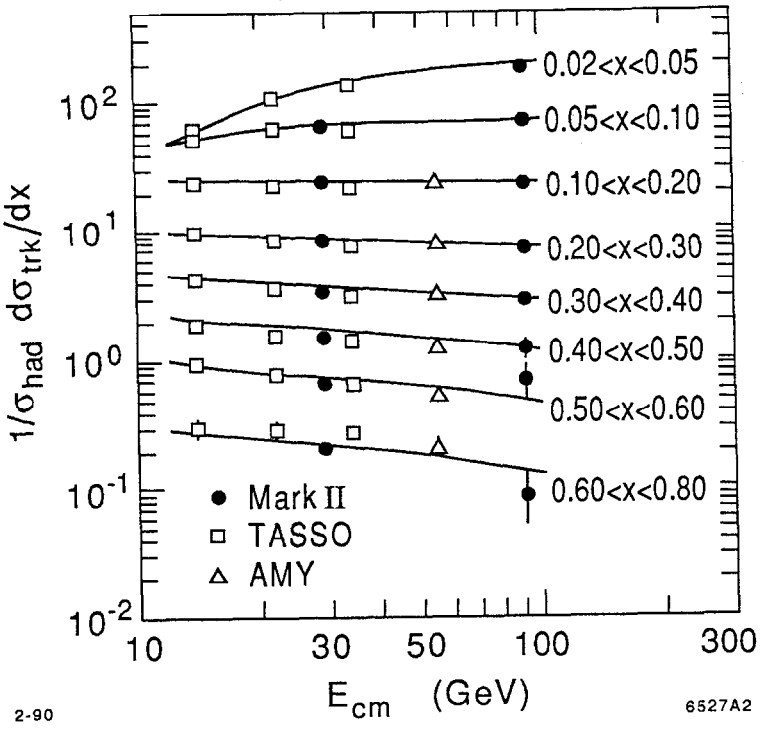

Figure 40: $1/\sigma\ d\sigma/dx$ for a given x for various E_{cm} values. The solid line is from the JETSET 6.3 shower model.

the increased energy available to produce soft particles. At the higher x range, the data points do show a scale breaking at a level that is consistent with the model predictions.

7.3 Transverse Momentum

As well as the absolute value of a charged particle's momentum, the direction of the particle also contains information. The sphericity axes described in Chapter 5 are used to define a coordinate system for an event. In general, two axes define a plane that contains most of the momentum of the event; the third axis is defined to make an orthogonal system. Individual track directions with respect to these axes were examined.

7.3.1 Variables

For each track, the components of momentum that are transverse to the sphericity axis were examined; the first lay in the event plane ($p_{\perp in}$) and the second lay out of the event plane ($p_{\perp out}$). As discussed in the chapter on event shapes, most of the events were planar. Therefore, the amount of transverse momentum out of the event plane given to an individual particle measures the effects of the fragmentation process. The fragmentation effect is also present for the transverse momentum in the event plane, but is overshadowed by gluon radiation. The sphericity axis usually lies along the direction of the most energetic quark and the gluon will have some $p_\perp$ with respect to that axis that is passed on to the fragmentation products. As the energy scale of the fragmentation is on the order of 1 GeV and gluons have energies up to $\approx$ 30 GeV (at $E_{cm} = 91$ GeV), the $p_\perp$ given by gluon radiation dominates.

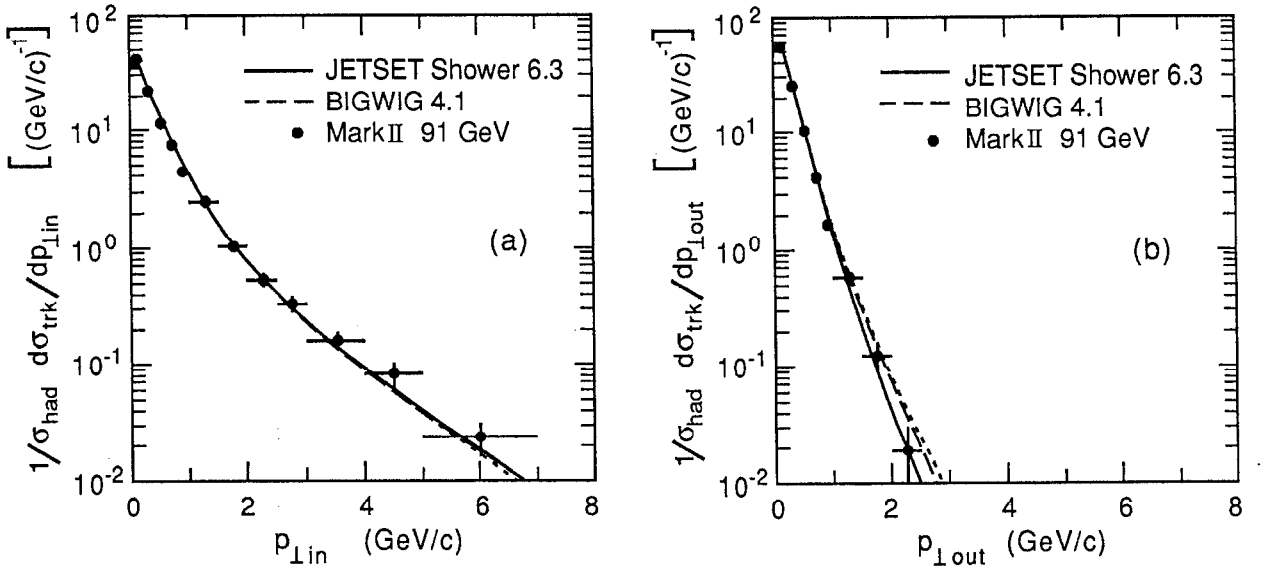

Figure 41: Distributions of transverse momenta (a) $p_{\perp in}$ and (b) $p_{\perp out}$.

The fragmentation effects are expected to change very slowly with changes in E_{cm}. On the other hand, the energy available for gluon radiation increases rapidly and so the $p_\perp$ in the event plane is expected to increase almost linearly. (The small decrease in the coupling constant α_s is a slight restraint on this effect.)

7.3.2 Results

The distributions were corrected in each bin and the result is shown in Figure 41 for the two variables. There is generally very little momentum out of the event plane, another indication that the sample consists of mostly 2– and 3–jet events. Again, the distributions are normalized to the number of hadronic events and the integrals are equal to the mean charged multiplicity. The error bars include statistical and systematic uncertainties, where the main systematic error came from variations in the correction factors from the models.

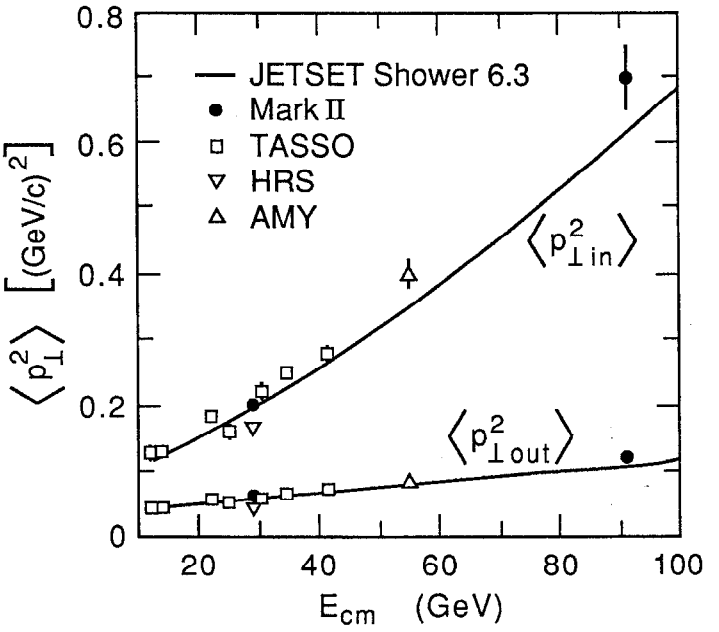

Figure 42: Mean of the squared transverse momentum distribution versus E_{cm}.

7.3.3 Variation with E_{cm}

To be able to compare with other experiments, the mean of the squared transverse momentum distributions, $<{p_{\perp in}}^2>$ and $<{p_{\perp out}}^2>$, were calculated. The values are $0.70 \pm 0.04 \pm 0.03$ and $0.121 \pm 0.004 \pm 0.003$, where the first error is statistical and the second systematic. The contributions to the systematic error for both cases were from model differences in the correction factors and variations when the p_{xy} cut was changed. In addition, the distributions both had tracks at high $p^2_\perp$ that contributed substantially to the mean. The weight of these tracks was varied to estimate another contribution to the systematic error.

These values, along with those from other experiments [24,61,62,64], are plotted in Figure 42. The solid line is the JETSET shower model result. As expected, the $<{p_{\perp out}}^2>$ shows only a small increase as E_{cm} increases. The transverse momentum

in the event plane does increase significantly. The prediction of the JETSET shower model is 2σ below what is observed. However, this is not a significant inadequacy of the models. It may be possible to find a parameter set that would give a result consistent with both the 91 GeV and the 29 GeV data values.

7.4 Rapidity

Again the particle's momentum with respect to the overall momentum flow in the event is used to give information. For this variable the thrust axes are used to define a coordinate system.

7.4.1 Variable definition

For each charged track, the rapidity y is defined as

$$y = \left| \frac{1}{2} \ln \frac{E + p_{||}}{E - p_{||}} \right|$$

where E is the particle energy and $p_{||}$ the component of momentum along the thrust axis. For all particles, the energy is calculated assuming a pion mass. The rapidity distribution is characterized by a broad plateau with a dip near $y = 0$ and a steep fall-off at high values. Changes in these characteristics with changes in E_{cm} are predicted by QCD: the plateau is expected to increase in height (as the multiplicity is increasing) and to broaden due to the increase in parton energy.

7.4.2 Results

The observed distribution was corrected using the bin-by-bin factors shown in Table 12. The result is shown in Figure 43 with the QCD models. We do see a slight

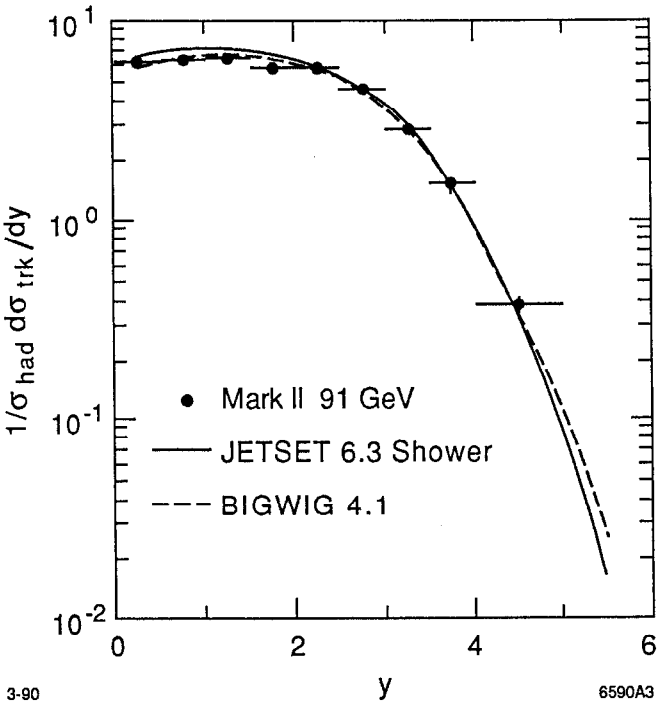

Figure 43: Corrected rapidity distribution.

dip at $y = 0$ and the broad plateau. The JETSET shower model overestimates the height of the plateau; this is associated with the difference in the charged multiplicities seen in section 7.1.

Chapter 8

Conclusions

Several of the distributions which characterize the hadronic decays of the Z^0 boson have been measured from the initial Mark II data sample. The shape distributions and the jet rates show that a majority of the events are 2–jet events, assumed to result from the decay of a Z^0 boson into a quark and an anti-quark. Some of the events, however, have a significant amount of momentum away from a single axis. The parton structure of these events is most likely $q\bar{q}g$, where the energetic gluon has been radiated from one of the quarks.

All measured quantities were corrected for detector effects and were compared with the predictions of two QCD–based Monte Carlo models. Both JETSET version 6.3 and BIGWIG 4.1 used parton shower generation for the perturbative region; the model for the fragmentation region was different. The model parameters were tuned at 29 GeV with the Mark II data from PEP. In all cases both models predicted distributions that were in agreement with the data distributions measured at $E_{cm} =$ 91 GeV.

The shape distributions that were measured were sphericity (S), thrust (1-T),

aplanarity (A), and the scaled invariant masses M_h^2/s and $(M_h^2/s - M_l^2/s)$. They each highlight different aspects of the events. The thrust is a good measure of the 2–jet events, whereas aplanarity is sensitive to 4–jet events and fragmentation effects. The mean values of each of these distributions were also compared to those from e^+e^- experiments at lower center-of-mass energies. The variation with E_{cm} shows that the events have a higher proportion of tightly collimated 2–jet events.

A study of two commonly used jet-finding algorithms was performed. It was found that the YCLUS algorithm, first used by the JADE experiment, reconstructed the quark directions and energies nearly as well as the LCLUS algorithm which is included in the JETSET model software. However, YCLUS showed a more consistent result with a changing center-of-mass energy and more events had the same number of reconstructed jets as initial partons. Using the YCLUS algorithm, the number of jets as a function of the jet resolution parameter y_{cut} was calculated. At a typical y_{cut} value of 0.04, there are 60% 2–jet events, 27% 3–jet events, and 3% 4–jet events. Also shown was the fraction of 3–jet events versus center-of-mass energy. The statistical error is too large to make any statement about the running of α_s.

Charged-particle inclusive distributions were also measured. An unfolding technique was used to obtain a corrected mean charged multiplitiy of $< n_{ch} >= 19.0 \pm 1.0(stat) \pm 0.9(sys)$. The scaled momentum distribution, when compared with lower energy e^+e^- annihilation data, showed slight scaling violations. The transverse momenta in and out of the event plane were calculated using the sphericity axes as the coordinate system. The mean values of the transverse momenta squared distributions were compared with values from lower E_{cm} experiments. The $< {p_{\perp in}}^2 >$ showed a rapid rise, indicating that harder gluons are being radiated in the event plane. The $< {p_{\perp out}}^2 >$ grew at a much slower rate, showing that the fragmentation effects are

not very energy-dependent. The last distribution measured was the rapidity y of the charged tracks. The data distribution has the expected characteristics.

Bibliography

[1] S. Weinberg, Phys. Rev. Lett. 19 (1967) 1264.

[2] G. Arnison *et al.*, Phys. Lett. B126 (1983) 398.

[3] P. Bagnaia *et al.*, Phys. Lett. B129 (1983) 130.

[4] G. S. Abrams *et al.*, Phys. Rev. Lett. 63 (1989) 724.

[5] D. Decamp *et al.* (ALEPH), Phys. Lett. B231 (1989) 519.
P. Aarnio *et al.* (DELPHI), Phys. Lett. B231 (1989) 539.
B. Adeva *et al.* (L3), Phys. Lett. B231 (1989) 509.
M. Z. Akrawy *et al.* (OPAL), Phys. Lett. B231 (1989) 530.

[6] G. Feldman *ed.*, *Proceedings of the Second Mark II Workshop on SLC Physics*, SLAC–Report–306, November, 1986.
G. Feldman *ed.*, *Proceedings of the Third Mark II Workshop on SLC Physics*, SLAC–Report–315, July, 1987.
J. Ellis and R. Peccei *eds.*, *Physics at LEP*, Vols 1 and 2, CERN 86–02, 21 Feb. 1986.

[7] F. Halzen and A. D. Martin, *Quarks and Leptons*, J. Wiley and Sons (1984).
D. H. Perkins, *Introduction to High Energy Physics*, Addison–Wesley (1987).

[8] S. L. Glashow, Nucl. Phys. 22 (1961) 579.

[9] A. Salam, 8$^{\text{th}}$ *Nobel Symposium*, N. Svartholm *ed.*, Almquist and Wiksell, Stockholm (1968) 367.

[10] G. S. Abrams *et al.*, Phys. Rev. Lett. 63 (1989) 2173.

[11] A. Barbaro-Galtieri, 8$^{\text{th}}$ *Workshop on $p\bar{p}$ Collider Physics*, LBL–28673, Feb. 1990. Recent limits of $m_t > 89$ GeV have also been reported but are not yet published.

[12] D. J. Gross and F. Wilczek, Phys. Rev. Lett. 30 (1973) 1343.
H. D. Politzer, Phys. Rev. Lett. 30 (1973) 1346.

[13] S. Komamiya *et al.*, Phys. Rev. Lett. 64 (1990) 987.

[14] P. Hoyer *et al.*, Nucl. Phys. B161 (1979) 349.
A. Ali *et al.*, Phys. Lett. 93B (1980) 155.

[15] W. Bartel *et al.* (JADE), Z. Phys. C21 (1983) 37.
W. Bartel *et al.* (JADE), Phys. Lett. B134 (1984) 275.
W. Bartel *et al.* (JADE), Phys. Lett. B157 (1985) 340.
H. Aihara *et al.* (TPC), Z. Phys. C28 (1985) 31.
M. Althoff *et al.* (TASSO), Z. Phys. C29 (1985) 29.
H. Aihara *et al.* (TPC), Phys. Rev. Lett. 57 (1986) 945.
P. Sheldon *et al.* (Mark II), Phys. Rev. Lett. 57 (1986) 1398.

[16] G. Ballochi and R. Odorico, CERN–EP/89–162, Dec., 1989.

[17] B. Andersson *et al.*, Phys. Rep. 97 (1983) 31.
X. Artru, Phys. Rep. 97 (1987) 1.
A. Casher, H. Neuberger, and S. Nussinov, Phys. Rev. D20 (1979) 179.
A. Casher, H. Neuberger, and S. Nussinov, Phys. Rev. D21 (1980) 1966.

[18] T. Sjöstrand, *Status of Fragmentation Models*, Int. J. Mod. Phys. A3 (1988) 751.
B. Bambah *et al.*, *QCD Generators at LEP*, CERN–TH–5466/89. July 1989.

[19] G. Marchesini and B. R. Webber, Nucl. Phys. B238 (1984) 1.
B. R. Webber, Nucl. Phys. B238 (1984) 492.

[20] G. Altarelli and G. Parisi, Nucl. Phys. B216 (1977) 298.

[21] W. Hofmann, in *Proceedings of International Symposium on Lepton and Photon Interactions at High Energies*, Hamburg, Germany (1987).

[22] T. Sjöstrand, Comput. Phys. Commun. 39 (1986) 347.
T. Sjöstrand and M. Bengtsson, Comput. Phys. Commun. 43 (1987) 367.
M. Bengtsson and T. Sjöstrand, Nucl. Phys. B289 (1987) 810.

[23] F. Gutbrod, G. Kramer and G. Schiergolz, Z. Phys. C21 (1984) 235.

[24] A. Petersen *et al.*, Phys. Rev. D37 (1988) 1.

[25] W. Braunschweig *et al.*, Z. Phys. C41 (1988) 359.

[26] B. Richter *et al.*, SLAC–PUB–4367, *1987 Lepton and Photon Symposium.*
SLAC–229, *Conceptual SLC Design Report*, June 1980.

[27] W. Farr *et al.*, Nucl. Instr. and Meth. 156 (1978) 283.

[28] G. Hanson, Nucl. Instr. and Meth. A252 (1983) 343.

[29] D. Briggs *et al.*, IEEE Trans. Nucl. Sci. NS-32 (1985) 653.

[30] D. Bernstein *et al.*, IEEE Trans. Nucl. Sci. NS-33 (1986) 86.

[31] H. Brafman *et al.*, IEEE Trans. Nucl. Sci. NS-32 (1985) 336.

[32] J. Perl *et al.*, Nucl. Instr. and Meth. A252 (1986) 616.

[33] J. Va'Vra *et al.*, Nucl. Instr. and Meth. 203 (1982) 109.

[34] G. S. Abrams *et al.*, Nucl. Instr. and Meth. A281 (1989) 55.

[35] G. S. Abrams *et al.*, IEEE Trans. Nucl. Sci. NS-25 (1978) 309.
G. S. Abrams *et al.*, IEEE Trans. Nucl. Sci. NS-27 (1980) 59.

[36] W. J. Willis and V. Radeka, Nucl. Instr. and Meth. 120 (1974) 221.

[37] E. Cisneros *et al.*, IEEE Trans. Nucl. Sci. NS-24 (1977) 413.

[38] M. Breidenbach *et al.*, IEEE Trans. Nucl. Sci. NS-25 (1978) 706.

[39] R. L. Ford and W. R. Nelson, EGS3, SLAC-210, June 1978.

[40] M. Nelson *et al.*, Phys. Rev. Lett. 50 (1983) 1542.

[41] M. E. Nelson, Ph.D. Thesis, LBL-16724mc, October 1983.
D. A. Karlen, Ph.D. Thesis, SLAC-325, March 1988.

[42] J. A. Kadyk, Proceedings of the Gas Sampling Calorimetry Workshop II, Batavia, IL, (1985) 373.

[43] R. C. Jared *et al.*, IEEE Trans. Nucl. Sci. NS-33 (1986) 916.

[44] J. Haggerty, Mark II/SLC Note #137 (1986), unpublished.

[45] H. Brafman *et al*, SLAC-PUB-2033, October 1977.

[46] T. Himel, SLAC-REP-223, October 1979.

[47] J. E. Grund, IEEE Trans. Nucl. Sci. NS-26 (1979) 220.

[48] R. Aleksan *et al.*, SLAC-PUB-4636, May 1988.

[49] Mark II Collaboration and SLC Final Focus Group, SLAC-SLC-PROP-2, April 1986.

[50] M. E. Levi *et al.*, Nucl. Instr. Meth. A281 (1989) 265.

[51] Iron-Nickel alloy with low thermal expansion coefficient.

[52] J. Seeman *et al.*, SLAC-PUB-3945, April 1986, published in proceedings LINAC86, 441.

[53] D. J. Nelson *et al.*, IEEE Trans. Nucl. Sci. NS-28 (1981) 336.

[54] J. E. Grund, IEEE Trans. Nucl. Sci. NS-27 (1980) 599.
J. S. Brown *et al.*, Nucl. Instr. and Meth. 221 (1984) 503.

[55] E. J. Siskind, IEEE Trans. Nucl. Sci. NS-30 (1983) 188.

[56] A. J. Lankford and T. Glanzman, IEEE Trans. Nucl. Sci. NS-31 (1984) 225.
T. Barklow *et al.*, IEEE Trans. Nucl. Sci. NS-33 (1986) 775.

[57] J. D. Bjorken and S. J. Brodsky, Phys. Rev. D1 (1970) 1416.
G. Hanson *et al.*, Phys. Rev. Lett. 35 (1975) 1609.

[58] E. Farhi, Phys. Rev. Lett. 39 (1977) 1587.
R. Brandelik *et al.*, Phys. Lett. B86 (1979) 243.

[59] G. S. Abrams *et al.*, Phys. Rev. Lett. 63 (1989) 1558.

[60] Ch. Berger *et al.* (Pluto), Z. Phys. C12 (1982) 297.
H. J. Behrend *et al.* (CELLO), Z. Phys. C44 (1989) 63.

[61] M. Althoff *et al.* (TASSO), Z. Phys. C22 (1984) 307.

[62] Y. K. Li *et al.* (AMY), KEK Preprint 89–149, Nov. 1989.

[63] W. Braunschweig *et al.* (TASSO), Z. Phys. C41 (1988) 63.

[64] D. Bender *et al.* (HRS), Phys. Rev. D31 (1985) 1.

[65] G. S. Abrams *et al.*, Phys. Rev. Lett. 63 (1989) 2447.
C. K. Jung *et al.*, Phys. Rev. Lett. 64 (1990) 1091.
M. Swartz *et al.*, SLAC–PUB–5176, Submitted to Phys. Rev. Lett.
P. R. Burchat *et al.*, SLAC–PUB–5172, Submitted to Phys. Rev. Lett.
S. Komamiya *et al.*, SLAC–PUB–5175, Submitted to Phys. Rev. Lett.

[66] R. Brandelik *et al.* (TASSO), Phys. Lett. B86 (1979) 243.
Ch. Berger *et al.* (Pluto), Phys. Lett. B86 (1979) 418.
D. P. Barber *et al.* (Mark J), Phys. Rev. Lett. 43 (1979) 830.
W. Bartel *et al.* (JADE), Phys. Lett. B91 (1980) 142.

[67] T. Sjöstrand, Comput. Phys. Commun. 28 (1983) 227.

[68] W. Bartel *et al.* (JADE), Z. Phys. C33 (1986) 23.
S. Bethke, Habilitationschrift, University of Heidelberg (1987) (unpublished).

[69] S. Bethke *et al.* (JADE), Phys. Lett. B213 (1988) 235.
W. Braunschwieg *et al.* (TASSO), Phys. Lett. B214 (1988) 286.
I. H. Park *et al.* (AMY), Phys. Rev. Lett. 62 (1989) 1713.

[70] G. S. Abrams *et al.*, Phys. Rev. Lett. 64 (1990) 1334.

[71] V. Blobel, in *Formulae and Methods in Experimental Data Evaluation*, Vol. 3, CERN (1984).

[72] C. Bacci *et al.* (Adone), Phys. Lett. B86 (1979) 234.
J. L. Siegrist *et al.* (Mark I), Phys. Rev. D26 (1982) 969.
B. Niczyporuk *et al.* (Lena), Z. Phys. C9 (1981) 1.
M. S. Alam *et al.* (Cleo), Phys. Lett. B49 (1982) 357.
Ch. Berger *et al.* (Pluto), Phys. Lett. B95 (1980) 313.
W. Bartel *et al.* (JADE), Z. Phys. C20 (1983) 187.
H. W. Zheng *et al.* (AMY), KEK-Preprint 90-5.

[73] M. Derrick *et al.* (HRS), Phys. Rev. D34 (1986) 3304.